

Figure I-5.1. r-z structure of an ILD quadrant.

## 5 Detector Layout and Technologies

Claude Vallee, Karsten Buesser  
1 pages

### 5.1 Overall structure of the detector

The geometrical structure of the ILD detector and the individual layouts of subdetectors were described in details in the ILD LOI [ref] and DBD [ref]. This section shortly reminds the main characteristics with emphasis on the recent evolutions and open options. The main design changes implemented since the DBD take into account continuous progress in detection technologies and the new optics of the ILC interaction region (chapter 3). In the following all dimensions are given for the large version of the detector (see section 4.2 for reduction factors of the small ILD).

Claude Vallee, Karsten Buesser  
1 pages

#### 5.1.1 Global structure and parameters

The overall ILD detector structure is shown in figure I-5.1: a high precision vertex detector positioned very close to the interaction point is followed by a hybrid tracking layout, realised as a combination of silicon tracking with a time projection chamber, and a calorimeter system. The complete system is located inside a large solenoid providing a nominal magnetic field of 3.5T (large ILD) or 4T (small ILD). On the outside of the coil, the iron return yoke is instrumented as a muon system and as a tail catcher calorimeter. The main geometrical parameters are summarised in table I-5.1 and table I-5.2.

**Table I-5.1.** List of the main parameters of the ILD detector for the barrel part.

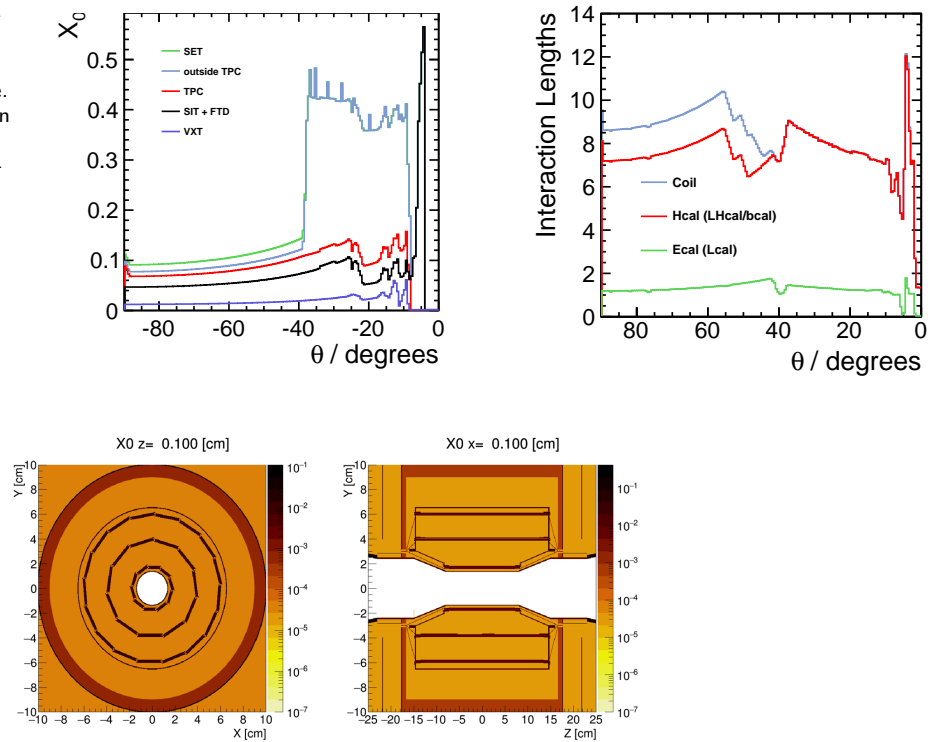
Barrel system						
System	R(in)	R(out)	z	comments		
		[mm]				
VTX	16	60	125	3 double layers layer 1: $\sigma < 3\mu m$	Silicon pixel sensors, layer 2: $\sigma < 6\mu m$	layer 3-6 $\sigma < 4\mu m$
Silicon						
- SIT	153	300	644	2 silicon strip layers	$\sigma = 7\mu m$	
- SET	1811		2300	2 silicon strip layers	$\sigma = 7\mu m$	
- TPC	330	1808	2350	MPGD readout	$1 \times 6\text{mm}^2$ pads	$\sigma = 60\mu m$ at zero drift
ECAL	1843	2028	2350	W absorber	SiECAL	30 Silicon sensor layers, $5 \times 5 \text{mm}^2$ cells
					ScECAL	30 Scintillator layers, $5 \times 45 \text{mm}^2$ strips
HCAL	2058	3410	2350	Fe absorber	AHCAL	48 Scintillator layers, $3 \times 3\text{cm}^2$ cells, analogue
					SDHCAL	48 Gas RPC layers, $1 \times 1 \text{cm}^2$ cells, semi-digital
Coil	3440	4400	3950	3.5 T field	$2\lambda$	
Muon	4450	7755	2800	14 scintillator layers		

**Table I-5.2.** List of the main parameters of the ILD detector for the end cap part.

End cap system						
System	z(min)	z(max)	r(min),	comments		
			r(max)			
	[mm]					
FTD	220	371		2 pixel disks 5 strip disks	$\sigma = 2 - 6\mu m$ $\sigma = 7\mu m$	
ETD	2420	2445	419- 1822	2 silicon strip layers	$\sigma = 7\mu m$	
ECAL	2450	2635		W-absorber	SiECAL ScECAL	Si readout layers Scintillator layers
HCAL	2650	3937	335- 3190	Fe absorber	AHCAL	48 Scintillator layers $3 \times 3\text{cm}^2$ cells, analogue
					SDHCAL	48 gas RPC layers $1 \times 1\text{cm}^2$ cells, semi-digital
BeamCal	3595	3715	20- 150	W absorber	30 GaAs readout layers	
Lumical	2500	2634	76- 280	W absorber	30 Silicon layers	
LHCAL	2680	3205	93- 331	W absorber		
Muon	2560		300- 7755	12 scintillator layers		

**Figure I-5.2**

Left: Average total radiation length of the trackers material as a function of polar angle. Right: Total interaction length seen up to the end of the electromagnetic calorimeter, the hadronic calorimeter and the solenoid coil, respectively.

**Figure I-5.3.** layout of the vertex detector.

A key characteristics of the detector is the amount of material crossed by the particles: particle flow requires a thin tracker to minimise interactions before the calorimeters, and thick calorimeters to fully absorb the showers and measure neutral hadrons. Figure I-5.2 shows the amount of radiation lengths of the trackers material and the total interaction lengths including the calorimeter system.

Subdetector technical conven-  
ers  
4 pages

### 5.1.2 Subdetector layouts

The current design of subdetectors is presented including open options and critical aspects, as well as prospects for enhanced capabilities in the future. The most recent progress and status of each detection technology will be summarized in section 5.2.

#### **Vertex detector** (*Besson, Ishikawa, Vos*)

The vertex detector (VTX, Figure I-5.3) is realised as a multi-layer pixel detector with three double-layers. The detector has a pure barrel geometry. To minimise the occupancy from background hits, the first double-layer is only half as long as the outer two.

Critical parameters of the VTX optimisation are the point resolution for secondary vertex tagging and the material thickness for minimal multiple scattering. Three main technologies are under consideration to achieve the required goals:

- **CMOS pixels:** this well-established technology offers the advantages of high granularity with fully monolithic pixel digital electronics available from industrial processes. The most critical

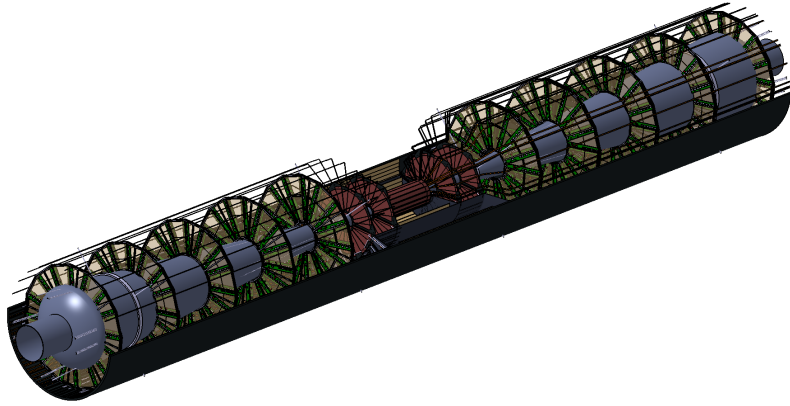


**Figure I-5.4.** layout of the Forward Tracking Detector.

points of focus of current R&D are the readout speed for bunch crossing tagging, the power consumption and the overall material budget of the layers.

- **DEPFET pixels:** this technology offers the advantage of high granularity with a small layer material thickness, the digital electronics being shifted at the end of the ladders. Critical aspects are the industrialisation of the fabrication process and the integration of large detector surfaces.
- **Fine Pixel CCD (FPCCD):** CCD's offer the prospects for the highest granularities associated with low power consumption. Another advantage is the minimal material budget of the detector layer, however counter-balanced by the need of a cryostat to ensure low-temperature operation. Critical aspects under study are the readout speed and the resistance to radiation.

The CMOS and DEPFET pixels have typical sizes of 20 microns and are readout in a continuous mode during bunch trains. The readout speed determines the capability to resolve individual bunches. The FPCCD pixels accumulate hits during one bunch train before readout and reset in-between trains. Their occupancy is kept acceptable thanks to a small pixel size of order 5 microns.

#### **Silicon trackers** (*Besson, Vos, Vila*)

A system of silicon trackers surrounds the VTX detector. In the barrel, two layers of silicon detectors (SIT) are arranged to bridge the gap between the VTX and the TPC, and one silicon outer layer (SET) is foreseen inbetween the TPC and the ECAL. In the forward region, a system of seven silicon disks (FTD) provides low angle tracking coverage (Figure I-5.4).

The baseline technology for the large area trackers is silicon strips but it is considered to move to pixel wherever possible: pixels are already the baseline for the two inner FTD disks, for which the current choice is DEPFET pixels. The possibility to equip more FTD disks with pixels is under study to improve track reconstruction efficiency in the forward region. The progress made with CMOS detectors may also allow to equip the SIT with pixels instead of strips. The design of the SET is still open including the option to implement it as the first layer of the ECAL Calorimeter. The use of high resolution timing detectors is considered in order to provide a TOF functionality for particle identification.

#### **TPC** (*Colas, Sugiyama*)

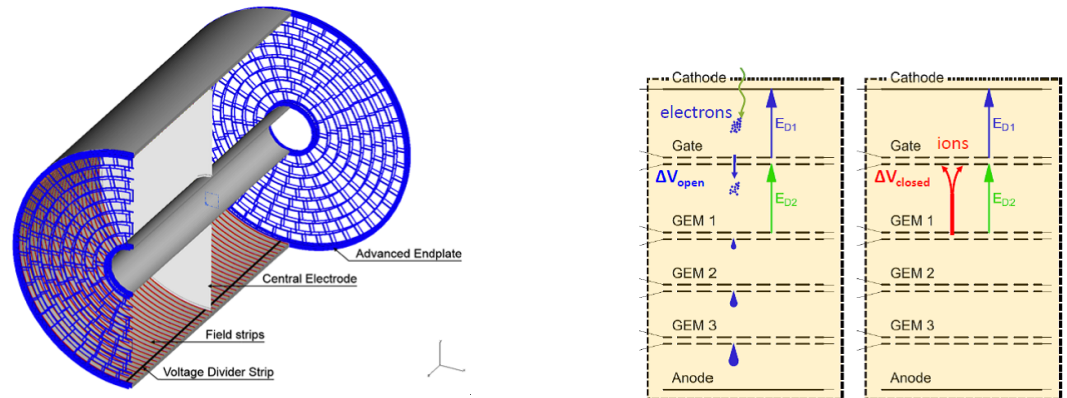


**Figure I-5.5.** Left: Global layout of the TPC chamber. Right: Principle of the ion GEM gating scheme showing the two electric field configurations within (left) and outside (right) bunch trains.

A distinct feature of ILD is a large volume time projection chamber (Figure I-5.5 left). The TPC advantages are 3-dimensional point resolution,  $dE/dx$  based particle identification and minimum material in the field cage. One critical issue concerns potential field distortions due to ion accumulation within the chamber. At ILC this can be mitigated by implementing an ion gating between bunch trains: ions produced in the gas amplification region during bunch trains are confined and eliminated outside bunch trains by reverting the electric field configuration. This can be implemented with GEM foils as shown in Figure I-5.5 right.

Three options are under consideration for the ionisation signal amplification and readout:

- GEM readout (Figure I-5.6 left): the ionisation signal is amplified by passing through a GEM foil and is collected on pads.
- Micromegas readout (Figure I-5.6 right): the ionisation signal is amplified between a mesh and the pad array where it is collected.
- GRIDPIX: the ionisation signal is amplified as for the micromegas case but collected on a fine silicon pixel grid providing individual pixel timing.

For the GEM and micromegas options, the typical pad sizes are a few mm (table I-5.1) and spatial resolution is improved by combining the track signals of several adjacent pads. For the GRIDPIX option the pixel size of  $\approx 50$  microns matches the size of the mesh, providing pixel sensitivity to single ionisation electrons. The spatial resolution is improved and the  $dE/dx$  signal measured by counting pixels.

### ECAL *(Brient, Ootani)*

Electromagnetic showers are measured with a compact highly-segmented calorimeter (Figure I-5.7) whose absorber planes are made of tungsten. The ECAL barrel shape is octagonal with individual stacks laid such as to avoid projective dead zones in azimuth. The baseline number of layers is 30, with options to reduce the number to 26 or even 22, keeping the amount of radiation lengths identical and increasing the thickness of the sensitive medium to maintain a similar energy resolution.

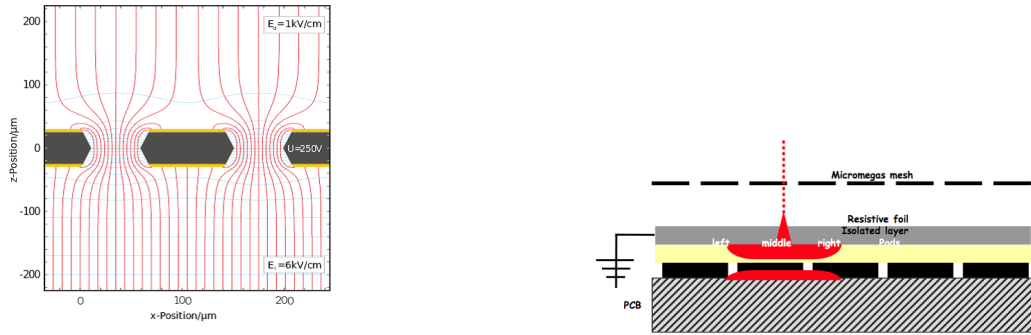


Figure I-5.6. Application scheme of the TPC ionisation signals with GEM (left) and micromegas (right) readout.

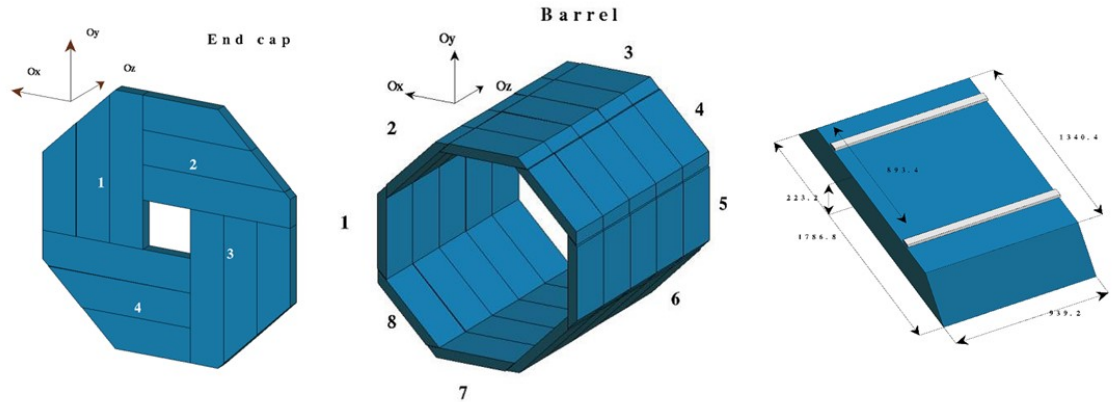


Figure I-5.7. Mechanical structure of the electromagnetic calorimeter: left: endcap wall; center: barrel; right: individual barrel stack.

The sensitive medium consists in silicon sensors with  $5 \times 5 \text{ mm}^2$  pads bonded on a PCB equipped with front-end readout ASICs (Figure I-5.8 left). In order to reduce the costs it is also considered to equip part of the sensitive layers with scintillator sensors readout through SiPMs (Figure I-5.8 left). In that case the scintillator strips would have a larger dimension of  $45 \times 5 \text{ mm}^2$  with alternate orthogonal orientation.

### HCAL (Laktineh, Sefkow)

The hadronic calorimeter consists in 48 longitudinal samples with steel absorber plates. Two options are currently considered for the mechanical structure, differing mainly in the barrel region

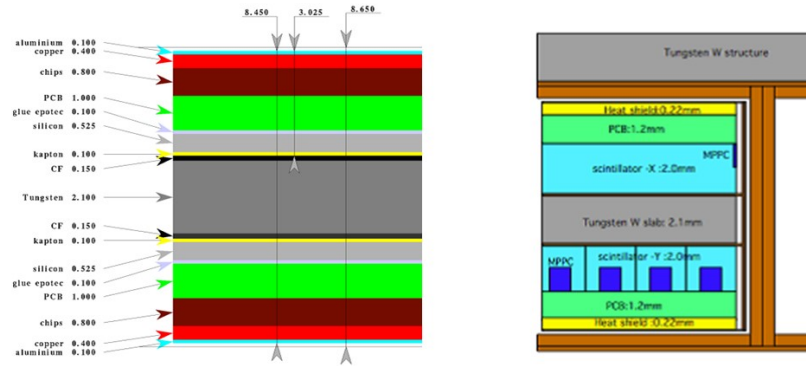


Figure I-5.8. ECAL sensitive layer: left: silicon option; right: scintillator option.

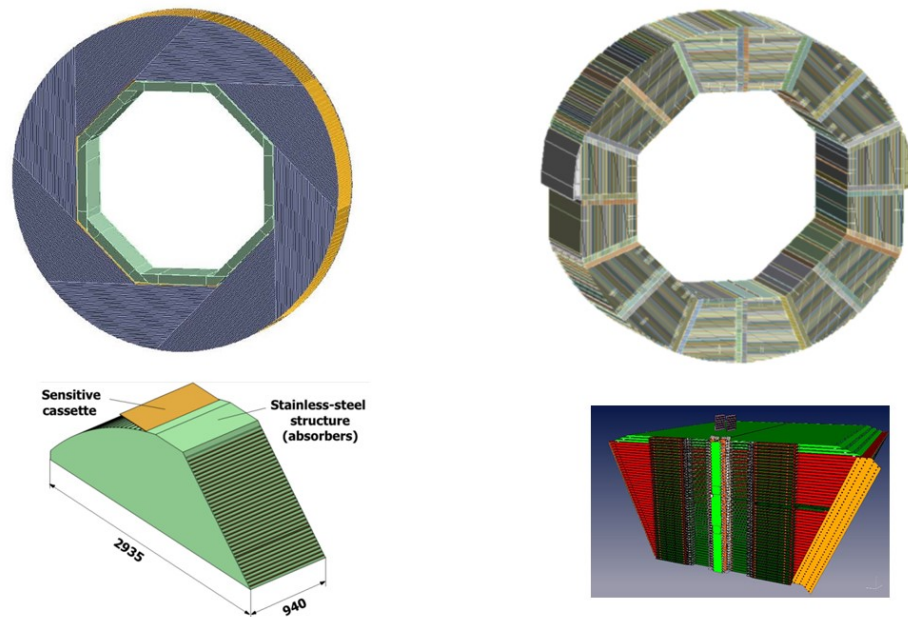


Figure I-5.9. HCAL barrel mechanical structure: full wheel (top) and individual stack (bottom) for the two configurations under consideration: the "Videau" option (left) and the "TESLA" option (right).

(Figure I-5.9): the "TESLA" barrel made of 2 wheels with signals extracted longitudinally in the gaps between the barrel and endcaps, and the "VIDEAU" barrel made of 3 to 5 wheels with signals extracted at the periphery between the HCAL and coil cryostat. The latter presents no projective dead zone in azimuth nor at  $90^\circ$  polar angle, and offers a better mechanical stiffness, at the cost of a reduced accessibility of the front-end electronics.

The HCAL layers are instrumented with high granularity for an efficient separation of charged and neutral hadronic showers, necessary for particle flow, as well as for a good muon identification for flavor jet tagging. Two sensor options are under consideration (Figure I-5.10): scintillator tiles of  $3 \times 3 \text{ cm}^2$  with analog readout through SiPMs, and RPC's with pads of  $1 \text{ cm}^2$  readout with a semi-digital

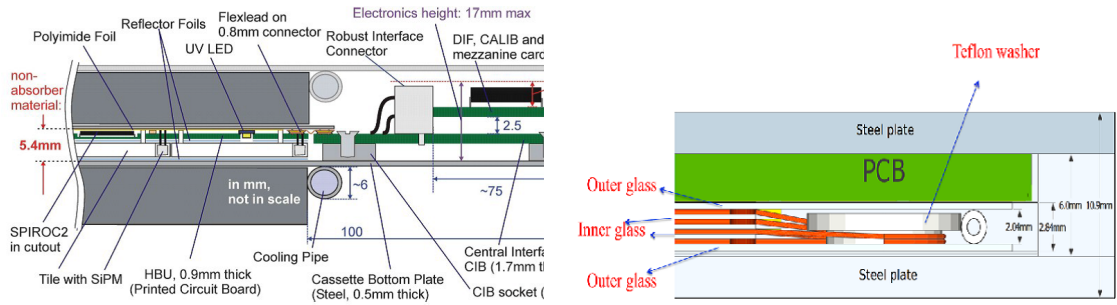


Figure I-5.10. HCAL sensitive layer; left: scintillator option; right: RPC option.

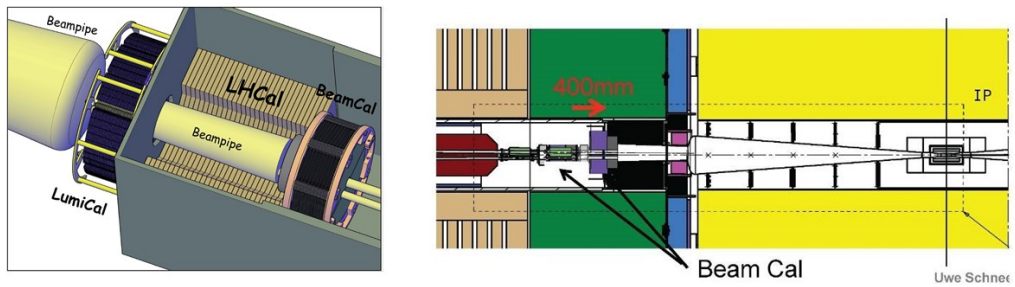


Figure I-5.11. Overall layout of the Very Forward detectors (left) and adaptations performed for the new ILC optics (right).

resolution of 2 bits.

**VFS** (Benhammou, Schuwalow)

The ILD very forward region is equipped with dedicated detectors to perform:

- a precise determination of the luminosity from Bhabha scattering electron pairs (LumiCAL);
- an extension of the hadronic calorimetry coverage in the forward region (LHCAL);
- calorimetric hermeticity down to the beam pipe and fast monitoring of beam conditions (BeamCAL).

The overall layout of the detectors is shown in Figure I-5.11 left. Their longitudinal positioning has been adapted as shown in Figure I-5.11 right to account for the new ILC optics (chapter 3).

The very forward detectors are based on similar technologies as the ILD electromagnetic calorimeter, taking into account the specific conditions of the forward region such as the harder radiation

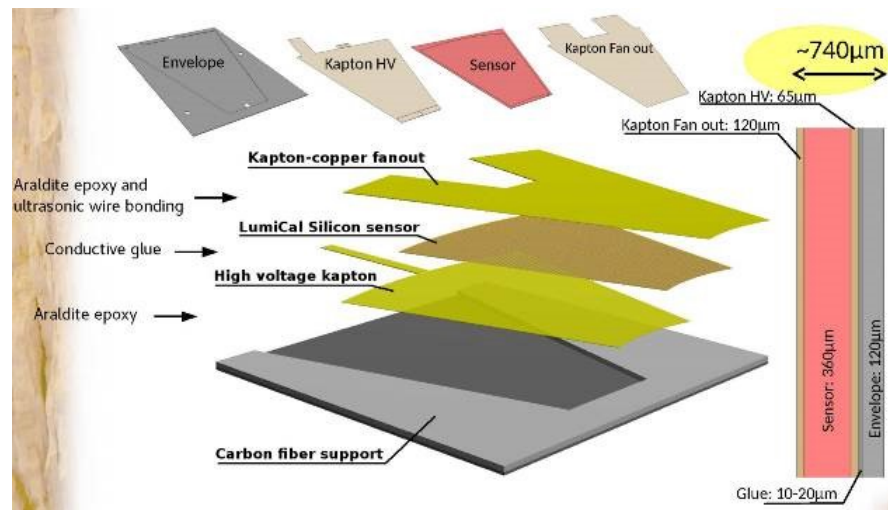


Figure I-5.12. Structure of a sensitive layer of the LumiCAL calorimeter.

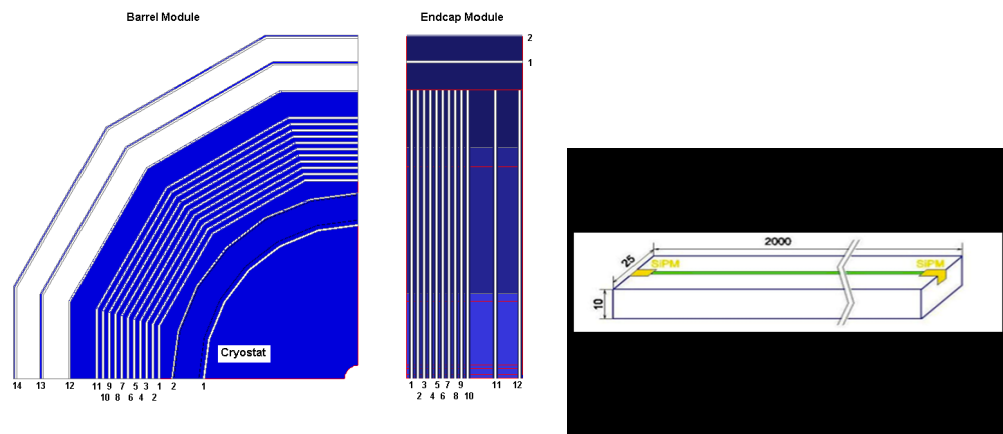


Figure I-5.13. Iron yoke baseline structure (left) and scintillator instrumentation option (right).

environment or the need for an improved compactness to identify electromagnetic showers in a high occupancy environment. For the detectors positioned closest to the beam pipe new sensors such as sapphire are considered. The LumiCAL has the most advanced design and will be based on silicon sensors similar to the ECAL (Figure I-5.12), with thinner instrumentation layers to minimize the lateral spread of the showers .

### Iron instrumentation (Saveliev)

A large volume superconducting coil surrounds the calorimeters, creating an axial  $B$ -field of nominally 3.5 Tesla (large ILD) or 4 Tesla (small ILD). An iron yoke returns the magnetic flux of the solenoid, and, at the same time, serves as a muon filter, muon detector and tail catcher calorimeter. The baseline structure of the yoke is shown in Figure I-5.13 left for a configuration accounting for the maximum stray fields allowed in the push-pull configuration (chapter 3). Optimisation of the yoke size is ongoing to minimize the overall cost driven by the amount of iron. A number of iron yoke gaps will be instrumented for muon tracking and measurement of the tails of the hadronic showers. The instrumentation is expected to consist in scintillator bars read with SiPMs (Figure I-5.13 right) but RPCs are also considered.

## 5.2 Subdetector technology status

All ILD detector technologies under consideration have benefited from substantial developments since the DBD publication. Many activities are coordinated within worldwide R&D Collaborations such as LCTPC [ref], CALICE [ref] or FCAL [ref]. Compared to the DBD studies, which were still focused on intrinsic physics response and performance, many technologies have now developed operational implementations with technological prototypes which are mature for extrapolation to a full detector. Applications have indeed already started with many spin-offs to existing experiments such as the high-luminosity LHC detector upgrades. The experience gained with these projects will be a strong asset to the final design and construction of ILD.

Auguste Besson, Akimasa  
Ishikawa, Marcel Vos  
3 pages

### 5.2.1 Vertex detector

The vertex detector is a high-precision small device which is expected to be one of the latest subdetectors to be built and inserted within ILD. The development of optimal technologies can therefore proceed until a few years before the start of ILC. There has been much progress in this direction in the past 5 years for the three main options under consideration: CMOS, DEPFET and FPCCD sensors.

**CMOS sensors:** The use of CMOS sensors for particle physics has benefited a lot from the development in the past two decades of the MIMOSA chip series by the IPHC Institute [ref]. A first full scale particle physics detector application has been realized with the STAR vertex detector (Figure I-5.14) on the RHIC hadron collider. Since then the technology has further developed as a widespread standard for pixel detectors, including many applications to e.g. LHC upgrades or new experiments.

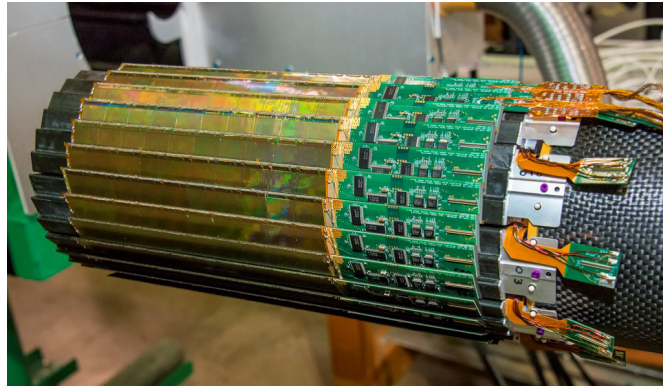
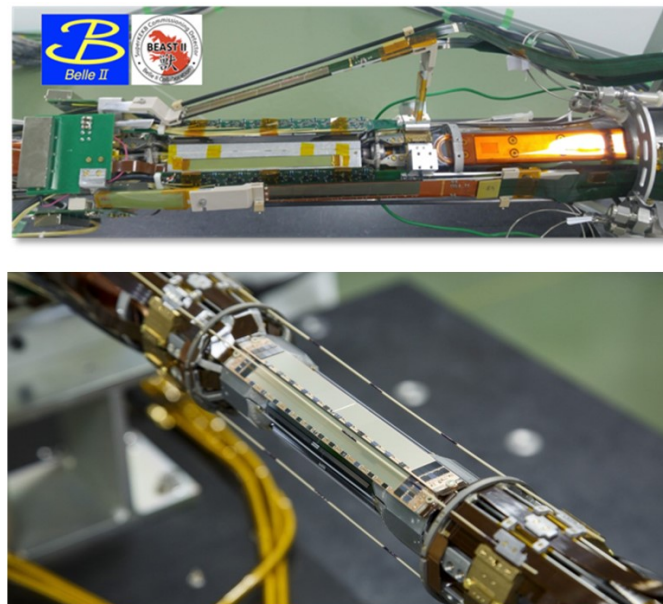
The general trend of performance improvements towards ILD specifications is summarized in table I-5.3. Compared to STAR the new applications for the ALICE upgrade and CBM at FAIR have moved to a technology with a smaller pattern, have implemented a new asynchronous readout scheme, and have improved the time resolution and power consumption to values close to ILD needs. The ALICE detector also concerns a very large area of more than  $10 \text{ m}^2$ , which qualifies the technology for the inner layers of a central tracker.

With these applications more attention is given to integration aspects of the technology. The chip intrinsic power consumption is now close to the ILD specification and could still be reduced by a factor 3 with power pulsing. To this respect a trade-off will have to be made between readout speed (related to time resolution) and power. With the expected heat production air cooling as done at STAR could be sufficient, but ILD has stronger constraints on the possible air flow due to a more forward instrumentation than STAR. This critical issue requires further studies. Low material ladder supports have been developed with the "PLUME" concept, consisting in a thin foam layer carrying pixel chips on both sides as a double layer [ref]. First PLUME ladders have been built and successfully operated for the BELLE II beam commissioning (Figure I-5.15 left).

**DEPFET sensors:** The development of DEPFET sensors in particle physics has been slower than that of CMOS but is also now reaching maturity. Following the demonstration of first operational ladders five years ago the technology has been chosen as the baseline for the BELLE II vertex detector, which can be seen as a 30% prototype of the ILC vertex detector. The initial integration difficulties of the technology which had led to delays in the BELLE II ladders assembly are now overcome: first

**Table I-5.3.** Development path of CMOS pixel sensors towards ILD.

DETECTOR:	STAR-PXL (ULTIMATE) 2014-16	ALICE-ITS (ALPIDE) 2021-22	CBM-MVD (MIMOSIS) 2021-22	ILD-VXD (PSIRA) 2030
Technology (AMS):	0.35 $\mu\text{m}$	0.18 $\mu\text{m}$	0.18 $\mu\text{m}$	< 0.18 $\mu\text{m}$ ?
Readout mode:	rolling shutter	asynchronous	asynchronous	asynchronous
Time resolution ( $\mu\text{s}$ ):	135	5-10	5	1-4
Power ( $\text{mW}/\text{cm}^2$ ):	150	35	200	50-100
Material ( $X_0/\text{layer}$ ):	0.39%	0.3%		0.15%

**Figure I-5.14.** The vertex detector of the STAR experiment based on the "ULTIMATE" CMOS pixel sensor.**Figure I-5.15.** Pixel detectors of the BELLE II experiment. Top: beam commissioning setup with "PLUME" CMOS (inclined sensors) and DEPFET (barrel) ladders; bottom: full inner layer of the BELLE II vertex detector equipped with DEPFET ladders.

DEPFET ladders have been successfully used in the BELLE II beam commissioning and the vertex detector full first layer is now in operation (Figure I-5.15). The full vertex detector is expected to be completed in 2020. Studies towards future BELLE II upgrades based on advanced DEPFET or CMOS technologies are now starting.

**FPCCD sensors:** The FPCCD technology is not yet used in full size detector applications but a first large prototype has been built [ref] with a sufficient size to cover the inner layer of the ILD

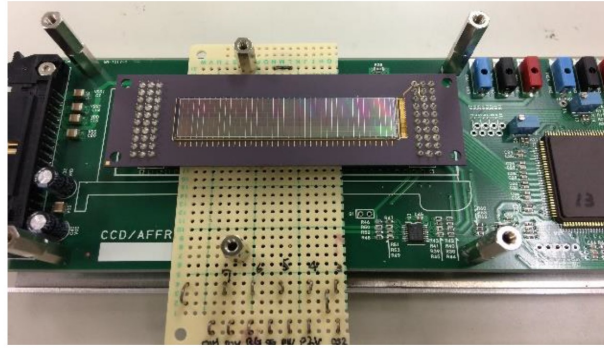


**Figure I-5.16.** First full size FPCCD ladder on its test bed.

vertex detector. The prototype is currently undergoing detailed characterization with e.g. radioactive source signals (Figure I-5.16). Irradiation tests of FPCCDs are also being performed since radiation hardness is a critical aspect of this technology.

(Besson, Vos, Vila)  
3 pages

### 5.2.2 Silicon trackers

Above DEPFET developments and FTD thermo-mechanical mockup

Paul Colas, Akira Sugiyama  
3 pages

### 5.2.3 Time projection chamber

The ILD TPC R&D is being conducted mainly within the LCTPC Collaboration [ref].

The workhorse for validation of detector prototypes and operational conditions is the TPC test set-up installed permanently in the DESY test beam (Figure I-5.17). The TPC stands within a magnet providing a magnetic field of 1 Tesla, and the beamline is equipped with precise incident and outgoing particle beam telescopes allowing to quantify the TPC reconstruction precision as function of the particle parameters. The beamtest set up is currently being upgraded with the high precision LYCORIS silicon telescope [ref], and a new TPC field cage with reduced field distortion is being assembled.

Significant progress has been seen in the manufacturing process of detection modules for each of the readout options. A new micromegas layout with resistive anodes has been shown to exhibit reduced boundary distortions [ref]. The flatness of the GEM modules has been improved significantly, increasing the gain uniformity by a factor 2 [ref]. Operational GridPix "QUAD" modules have been built based on the TimePix3 pixel chip [ref]. Recent prototypes of the three types of detection modules are shown in Figure I-5.18.

The performance of the three technologies has been measured in beam tests. Figure I-5.19 shows that the target goals of a spatial resolution better than 100 microns and of a  $dE/dx$  resolution better than 5% have been reached in all cases.

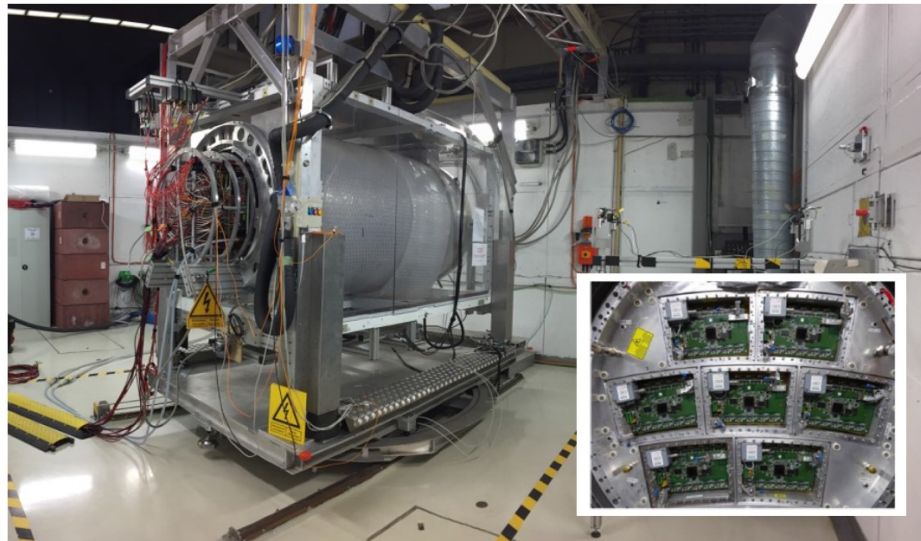


**Figure I-5.17.** The TPC test setup at DESY. The insert shows the geometrical structure of the TPC endcap which can host prototypes of detection planes.

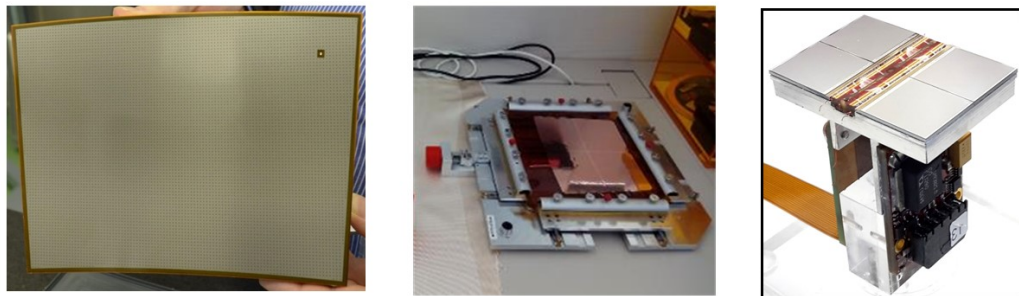


**Figure I-5.18.** TPC prototype detection modules for the three baseline technologies under consideration: microegas module (left), GEM module (middle) and GridPix QUAD module (right).

Two critical aspects of a TPC operation consist in the cooling of the readout endcaps, which must be realized with minimal dead material, and the mitigation of the drift field distortions which may develop from the accumulation of ions in the drift volume. For the first point a double phase  $CO_2$  cooling system with thin low-material fluid pipes has been developed and shown to perform adequately (Figure I-5.19 left). For the second point an ion gating scheme based on GEM foils has been implemented and beam tested. Results show that a good transparency for drift electron signals can be maintained while preventing the accumulation of ions in the drift volume (Figure I-5.19 right).

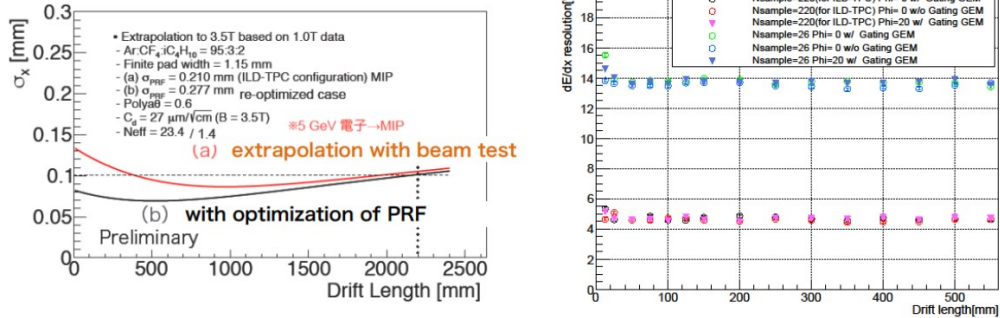


Figure I-5.19. Resolution on the track position (left) and ionisation loss  $dE/dx$  (right) as function of the drift length, for the three readout options under consideration (figures to be updated with inclusion of the 3 technologies)

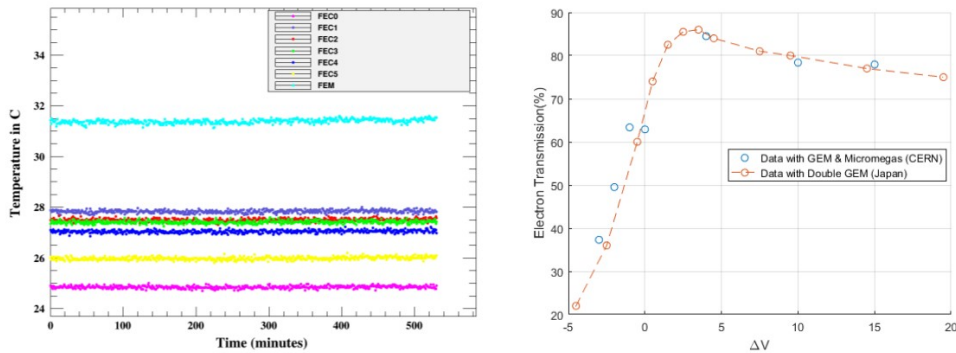


Figure I-5.20. TPC operation achievements: temperature stability with double phase CO<sub>2</sub> (left) and electron transparency with GEM gating (right).

Jean Claude Brient, Wataru Ootani  
3 pages

### 5.2.4 Electromagnetic Calorimeter

In the past 5 years the Silicon option of the electromagnetic calorimeter has focused on the design and construction of technological prototypes of the detector including beam tests. A fully integrated layout of the detection board has been designed with the required dimension of  $16 \times 16 \text{ cm}^2$  corresponding to 1024 channels (Figure I-5.21 top). The board hosts 16 SKIROC ASICs developed by OMEGA [ref] to process 64 channels each. A calorimeter prototype based on 10 such detection layers has been built (Figure I-5.21 bottom) and beam-tested on several occasions at DESY and CERN, including a combined test with a SDHCAL prototype of the hadronic calorimeter (next section).

The response of this technological prototype to particles behaves as expected. A signal-to-noise ratio of 20 is measured for MIPs in single pads (Figure I-5.22 left). Such a large MIP signal is

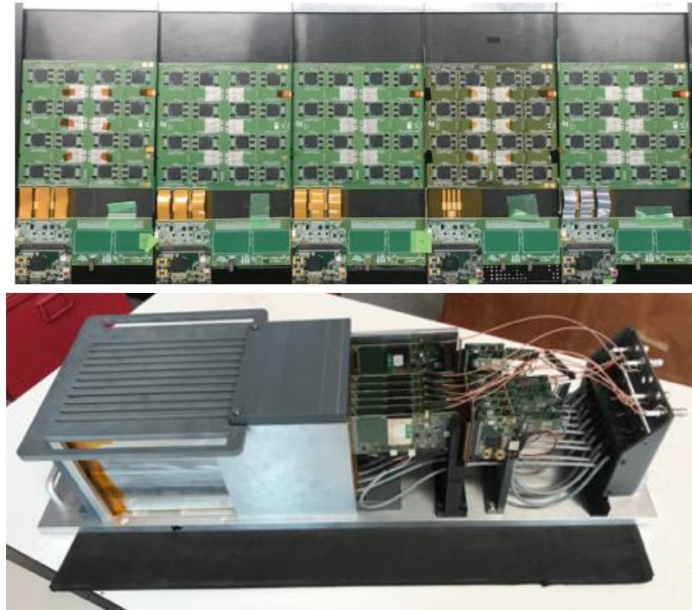


**Figure I-5.21.** Technological prototype of the SiW ECAL. Top: set of integrated sensor&readout boards; bottom: 10-layers calorimeter prototype used in beam tests at DESY and CERN.

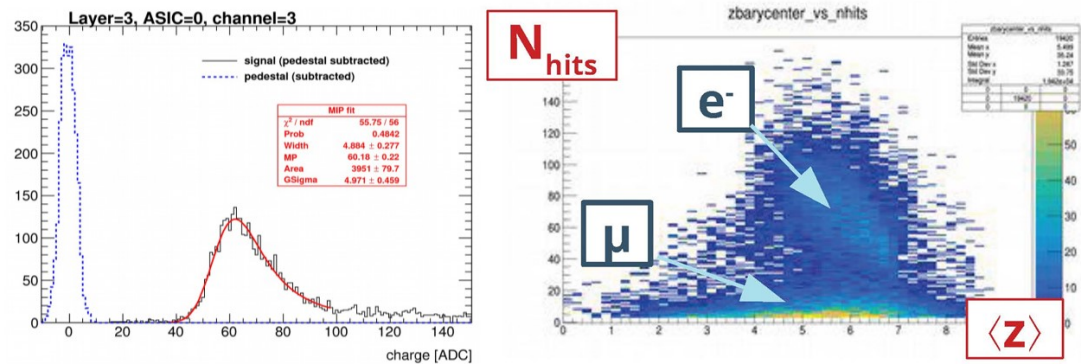


**Figure I-5.22.** Particle response of the SiW ECAL prototype: MIP response of a single pad (left) and shower profile of muons and 80 GeV electrons (right).

important for isolated particle identification in particle flow energy reconstruction. First response to high energy electrons has recently been measured at CERN in a combined test with the SDHCAL (Figure I-5.22 right). More detector slabs are currently in construction to reach a total number of 20 detection layers required to fully contain electromagnetic showers. This will allow measurements of the energy resolution. The beam tests have also been used to validate the power pulsing of the front-end electronics required to minimize heat production within the calorimeter.

More developments are ongoing to reach the requirements of the full-size ILD detector. A large detector slab with dimensions similar to those of the calorimeter modules has been built and tested with MIP particles (Figure I-5.23 right). A 10% signal drop has been observed along the full length of the slab and could be attributed to power voltage drops and clock reflections. An updated long slab

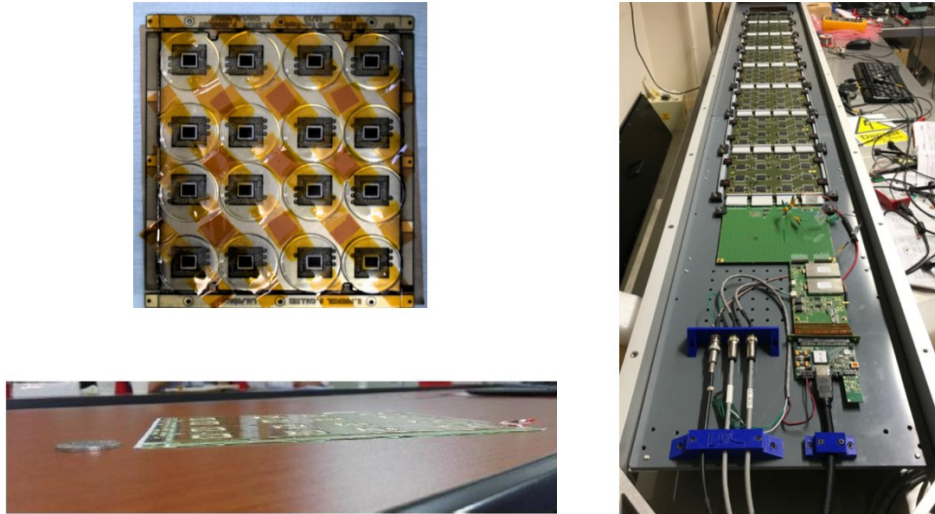


**Figure I-5.23.** SiW-ECAL developments towards the final detector: thin chip-on-board sensors (left) and long slabs corresponding to ILD dimensions (right).

is under construction to correct these effects and validate the solutions. Ultra thin detection boards with ASICs integrated within the PCB have also been developed and are under test with cosmics (Figure I-5.23 left). They may allow even more compact layouts of the electromagnetic calorimeter.

It is worth reminding that the Silicon technology developed for ILD has been retained as the baseline for the electromagnetic section of the CMS High Granularity Calorimeter (HGCAL) upgrade [ref]. The HGCAL layout is based on hexagonal readout modules with a technology similar to the ILD one. It incorporates a new version of the SKIROC ASIC with a  $\approx$ ns timing functionality which may also be of interest for the ILD detector. A HGCAL prototype of 27 layers has been successfully tested by CMS in a combined beam test at CERN with the AHCAL ILD prototype (next section). The full HGCAL represents a 10% prototype of the ILD SiW ECAL as regards the number of channels. Its construction will be a strong asset to validate the large scale assembly and fabrication processes for ILD.

*Sc-ECAL results from new detector unit in construction.*

Felix Sefkow, Imad Laktineh  
4 pages

### 5.2.5 Hadronic Calorimeter

*AHCAL beamtest results from large technological prototype, CMS HGCAL spinoff.*

The SDHCAL technological prototype built in 2011 has been regularly tested in beams in the past years with various configurations [ref], including a combined test with the SiW-ECAL prototype in 2018 (previous section). The SDHCAL prototype consists in 48 single-gap RPC layers of  $1 \text{ m}^2$  (Figure I-5.24). Each detection gap is instrumented with 6 Active Sensitive Units (ASU) made of a  $50 \times 33 \text{ cm}^2$  PCB with 24 "HARDROC" ASICs from OMEGA [ref]. The RPC pad size is  $1 \text{ cm}^2$  and the pad signals can be readout either in digital (1 bit and 1 threshold) or semi-digital (2 bits and 3 thresholds) modes.

The numerous data sets collected at CERN with high-energy hadron beams have been used to

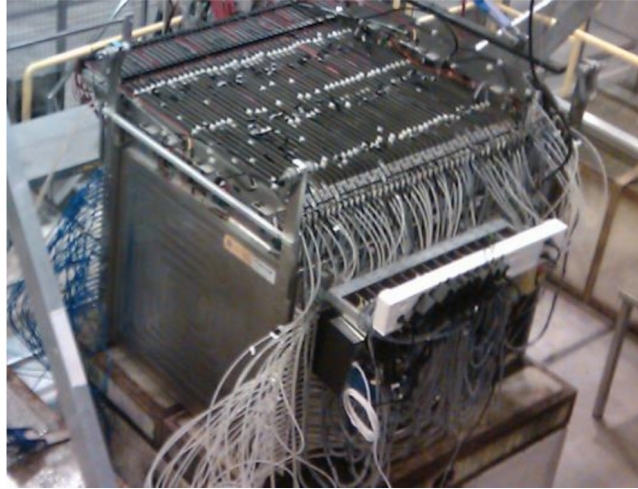


Figure I-5.24. Technological prototype of the Semi-Digital Hadronic Calorimeter.

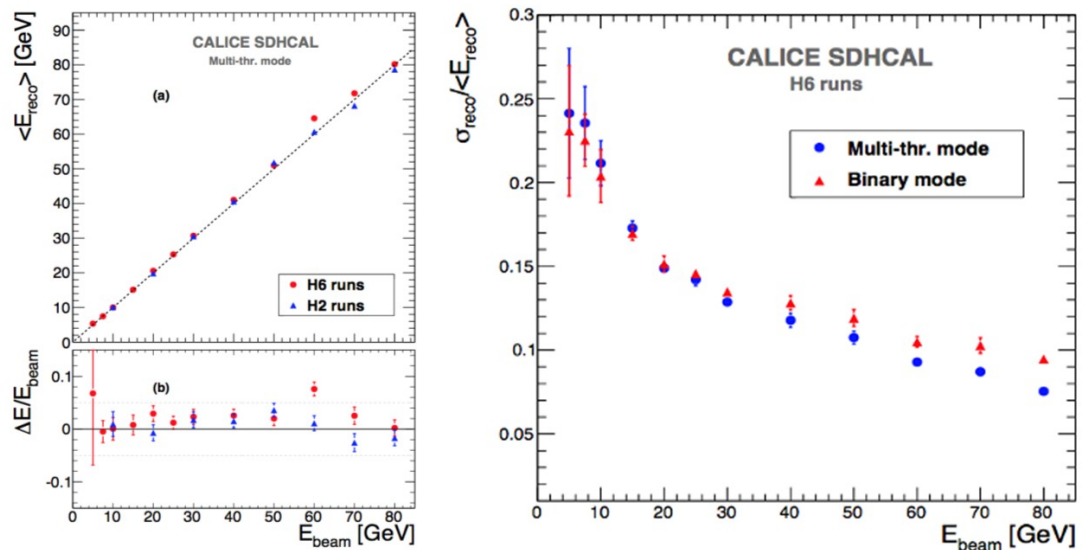
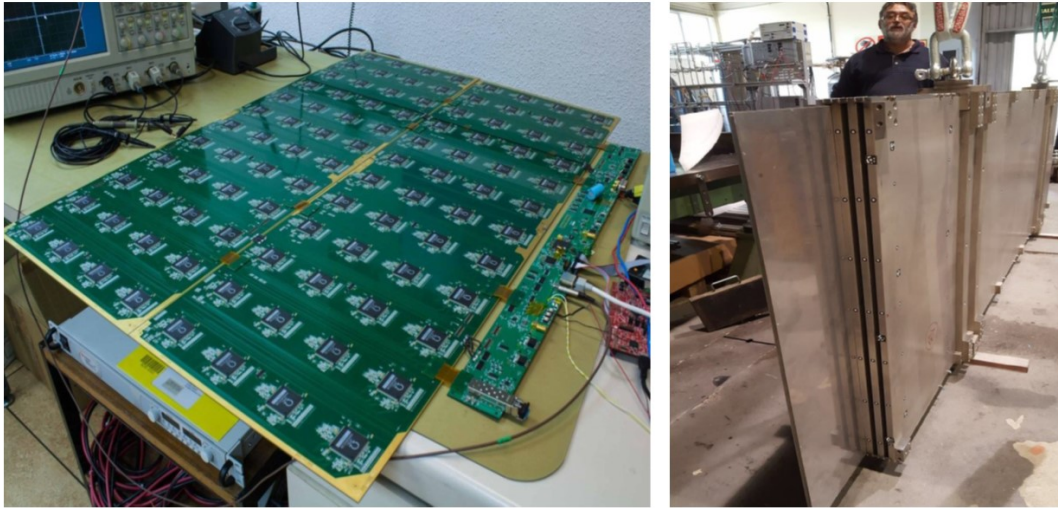


Figure I-5.25. Performance of the SDHCAL technological prototype as measured in beam tests: linearity (left) and energy resolution for the digital and semi-digital readout options (right).

validate the performance of the technology. Special reconstruction methods adapted to the high granularity semi-digital structure of the calorimeter have been developed [ref] to relate the energy estimation to the hit number and density. The current state of the performance is summarized in Figure I-5.25. A good linearity is observed and the multi-threshold mode is found to mitigate saturation and improve the resolution at high energy. The description of the measured resolution by the simulation is however found to be sensitive to the description of the core of the hadronic showers, with a tendency for the Monte-Carlo to underestimate the performance due to harder cores in the showers. This point will require further tuning of the simulation.

In the recent years the SDHCAL teams have focused on adapting the technology to the full-size ILD requirements, in order to cover detection surfaces of up to  $1 \times 3 \text{ m}^2$  required by the ILD Hadronic Calorimeter in its "Videau" configuration (section 5.1.2). An improved RPC gas circulation system with better uniformity has been designed and validated with the construction of two large RPC's. Larger ASUs of  $100 \times 33 \text{ cm}^2$  have been designed with a new version of the HARDROC ASIC including 0-suppression (Figure I-5.26 left), and their interconnection improved to allow chaining of



**Figure I-5.26.** SDHCAL ongoing developments for the final ILD dimensions: two active sensor units of  $100 \times 33 \text{ cm}^2$  chained to each other and connected to the outside with a new compact DAQ interface (left), and self-sustained welded structure of 4 calorimeter plates of  $1 \times 3 \text{ m}^2$  with the required mechanical tolerances (right).

up to 9 ASUs. Efforts have also been invested in the manufacturing process of self-sustained hadron calorimeter structures with high precision mechanical tolerance as required by the RPC insertion. A new method of "roller levelling" has been developed to machine steel absorber plates with a high flatness. A high precision electro-welding has been used to built a first large size prototype of 4 calorimeter layers (Figure I-5.26 right) which has proven that gap size variations well below 1 mm can be reached on such large structures.

For the longer term the option of multi-gap RPC's with a high timing resolution of  $\approx 20 \text{ ps}$  is prototyped based on the "PETIROC" ASIC [ref].

Yan Benhammou, Sergej  
Schuwalow  
2 pages

## 5.2.6 Very forward detectors

In the past years the development of the ILD forward detectors has mostly been pursued by the FCAL R&D Collaboration [ref]. Progress concerns mainly the LUMICAL calorimeter and, more recently, the BEAMCAL sensors.

Based on a specific ASIC [ref] developed after the DBD, calorimeter silicon sensitive layers have been built to assemble a first LUMICAL 4-layer tungsten calorimeter prototype and, two years later, a more compact 8-layer calorimeter prototype (Figure I-5.27 left). The two prototypes were beam-tested in 2014 and 2016, respectively. The test data [ref] confirm the expected significant improvement of the transverse compactness of the electromagnetic showers in the compact prototype compared to the earlier one (Figure I-5.27 right).

A new ASIC "FLAME" [ref] based on 130 nm CMOS technology is currently under final validation. FLAME features the low power, in-situ digitisation and fast readout required by the final detector. A new  $\approx 20$ - layers SiW calorimeter prototype based on FLAME, with specifications and configuration close to the final LUMICAL detector, is under construction and planned to be beam-tested in 2019.

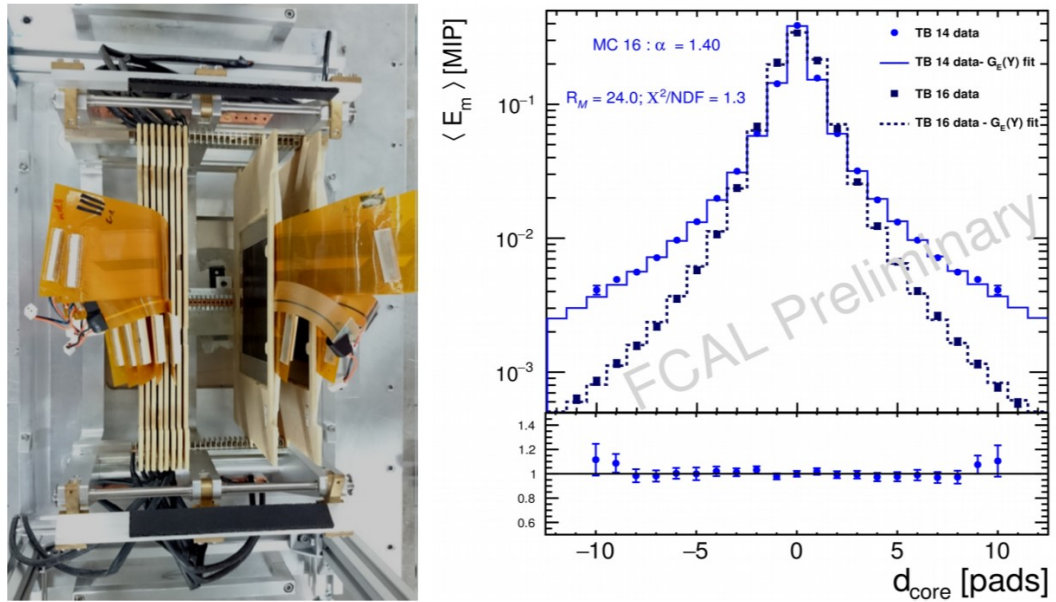


**Figure I-5.27.** LUMICAL compact prototype tested in the DESY electron beam in 2016 (left) and corresponding improvement in shower compactness achieved versus the 2014 prototype (right).

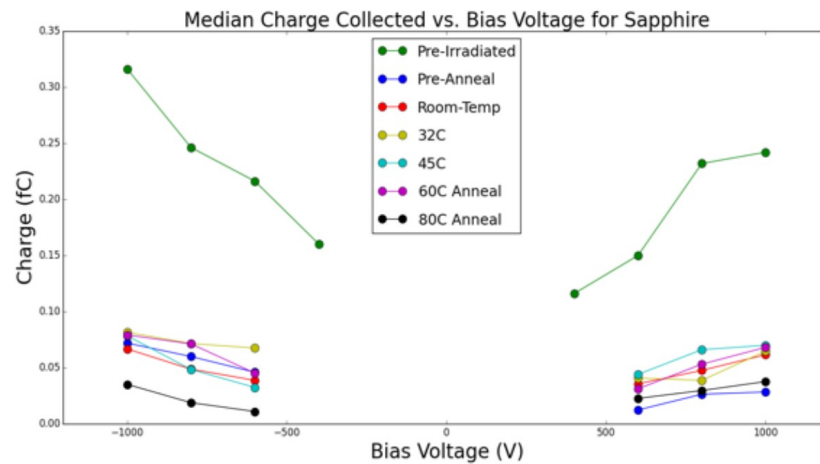


**Figure I-5.28.** results of irradiation tests performed at SLAC for sapphire sensors considered for the BEAMCAL.

The LHCAL and BEAMCAL calorimeters can be based on similar technologies as the LUMICAL, with radiation hardness requirements increasing as function of the sensor proximity to the beam. For the BEAMCAL, new sensors such as sapphire are being considered. Irradiation campaigns are under way to characterize them (Figure I-5.27 right) and provide input for the final choice.

Valery Saveliev

1 pages

### 5.2.7 Iron instrumentation

Dedicated studies have been conducted at FNAL in the past years to optimize the layout of scintillator bars adapted to muon detection. Prototypes have been built and tested with muon beams [ref]. They are all based on long scintillator bars with signal collected by WLS fibers and readout by SiPMs at both extremities. The transverse resolution of  $\approx 1\text{cm}$  required for the muon momentum measurement is

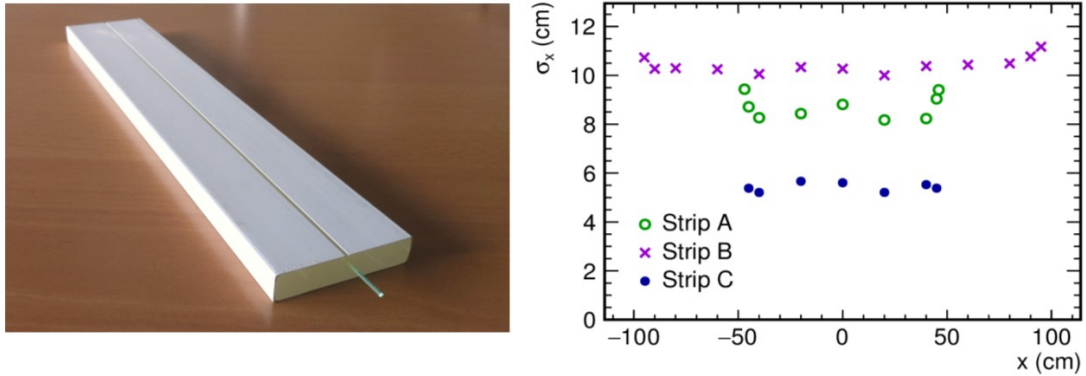


**Figure I-5.29.** Left: example of prototype scintillator bar built for the muon detector; right: longitudinal resolution on reconstructed muon as function of longitudinal coordinate: strip A and B as on left figure with lengths of 1 and 2 m respectively, strip C of 1m length with WLS fibers positioned on the small edge of the strip.

defined by the bar widths of a few cm. The longitudinal position is measured from the time difference of the signals of both extremities and depends on the WLS configuration. Two configurations have been tested: strips "A" and "B" with the WLS fibers positioned in an extruded groove at the center of the large side of the bar (Figure I-5.29 left); strip "C" with a set of WLS fibers positioned along the small edge of the bar. Longitudinal resolutions of 5 to 10 cm are measured and found roughly independent of the longitudinal position of the muon within the bar (Figure I-5.29 right).

More studies are ongoing to develop low cost SiPMs also adapted to the measurement of the tails of high energy jets (tail catcher function).

The RPC option for the iron yoke instrumentation was not specifically studied but would directly benefit from the RPC developments of the SDHCAL hadronic calorimetry option (section 5.2.4).

# 6 ILD Global Integration

Karsten Buesser, Claude Vallee

pages

Karsten Buesser, Roman Poeschl, Toshiaki Tauchi

3 pages

## 6.1 Internal ILD integration

Subdetector interfaces and integration scheme including services. Short reminder of the overall ILD integration scheme (unchanged). Technical drawings (ideally from CAD files) showing interfaces (pipes, cables, supports) for each subdetector within ILD. New input is expected from the recently setup dedicated working group chaired by Roman to update the service paths based on subdetector Interface and Control Documents.

Among points to illustrate: Inner tracker services, TPC services, ECAL electrical interfaces, HCAL interfaces in TESLA option and Videau option, VFS cables, global scheme for cable paths.

Yasuhiro Sugimoto

1 pages

## 6.2 External ILD integration

Generic layout of the cavern, mentioning the current options for its configuration (TDR, Tohoku, YS).

### 6.2.1 Site-related Infrastructure

The proposed site for the ILC is located in the Kitakami mountains in the north of the Japanese main island Honshu. Dedicated studies are under way to adapt the generic ILC design, as described in the Technical Design Report, to the realities in this environment. For ILD, the arrangements of the surface and underground installations around the interaction point (IP) are of natural importance. The current conceptual design of the civil facilities and the plans for the detector related infrastructure and services have been coordinated between the relevant detector and ILC matching groups as well as with local experts.

ILD will be assembled on the surface, similar to CMS at LHC. Figure I-6.1 shows a rendering of the surface installations above the ILC interaction point. At the heart is the detector assembly building that is located directly over the central shaft that gives access to the underground collider hall. A large gantry crane above the shaft allows for the lowering of the pre-instrumented detector parts into the underground area. A preparation building is foreseen where sub-detector elements can be assembled and tested. A research building and a computing building provide the infrastructure for the operation of the detectors at the IP Campus.

The underground experimental hall is about 100 m below the surface and hosts two experiments, ILD and SiD, in a "push-pull" arrangement (c.f. I-6.2). Both detectors share one interaction region and are installed on movable platforms and can be rolled into or out of the beam line within a few hours. The detectors can be opened and maintained in their parking positions. Access to the underground

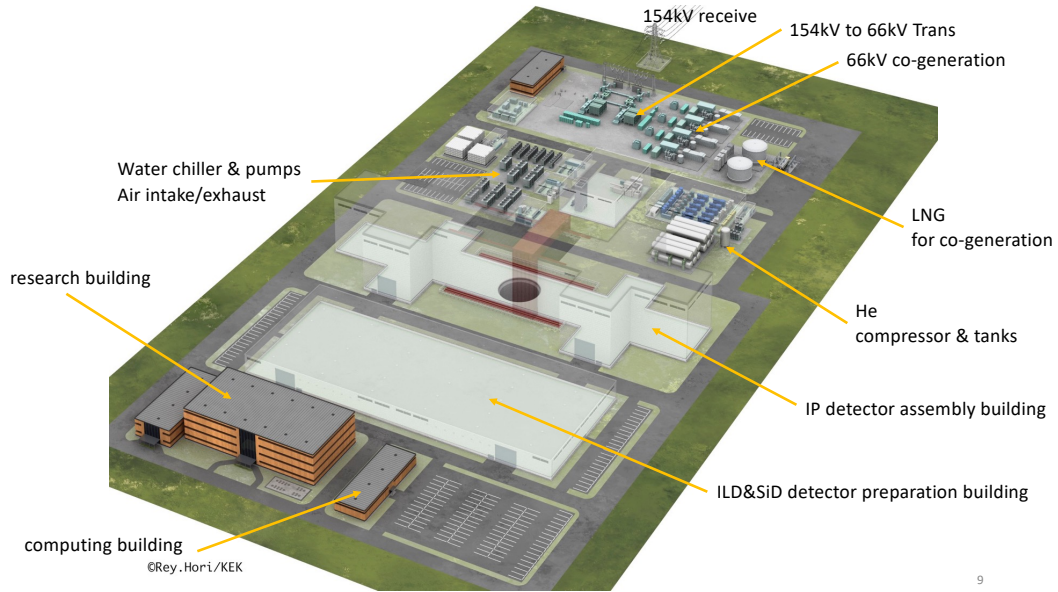


**Figure I-6.1.** Conceptual design (artist's view) of the surface facilities ("IP Campus") above the ILC interaction point [3].

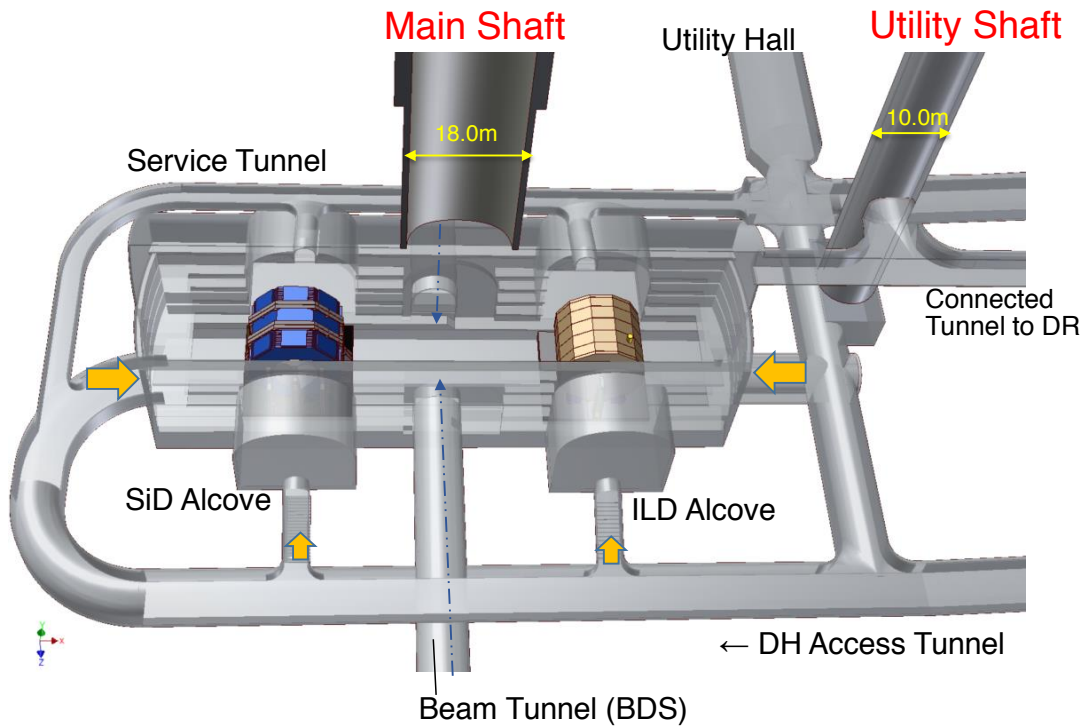


**Figure I-6.2.** Underground facilities with the detector hall, ILD and SiD in push-pull configuration, access tunnels and shafts [4].

hall is provided by two vertical shafts and an access tunnel that allows for vehicles to drive directly into the underground area I-6.3.

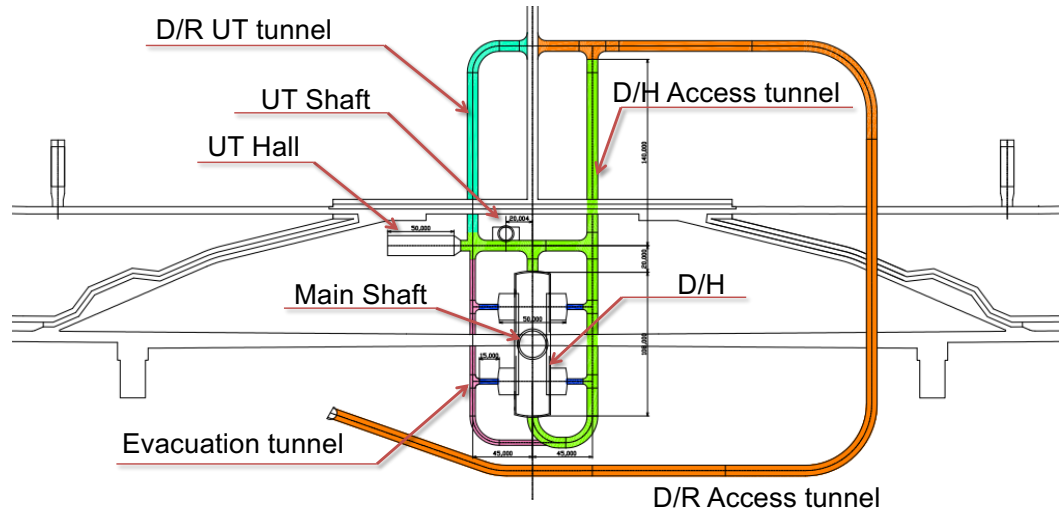


**Figure I-6.3.** Access to the underground infrastructure is provided by two shafts, main shaft and utility (UT) shaft, and a system of access tunnels [5] that serve the detector hall (DH) as well as the damping rings (DR).

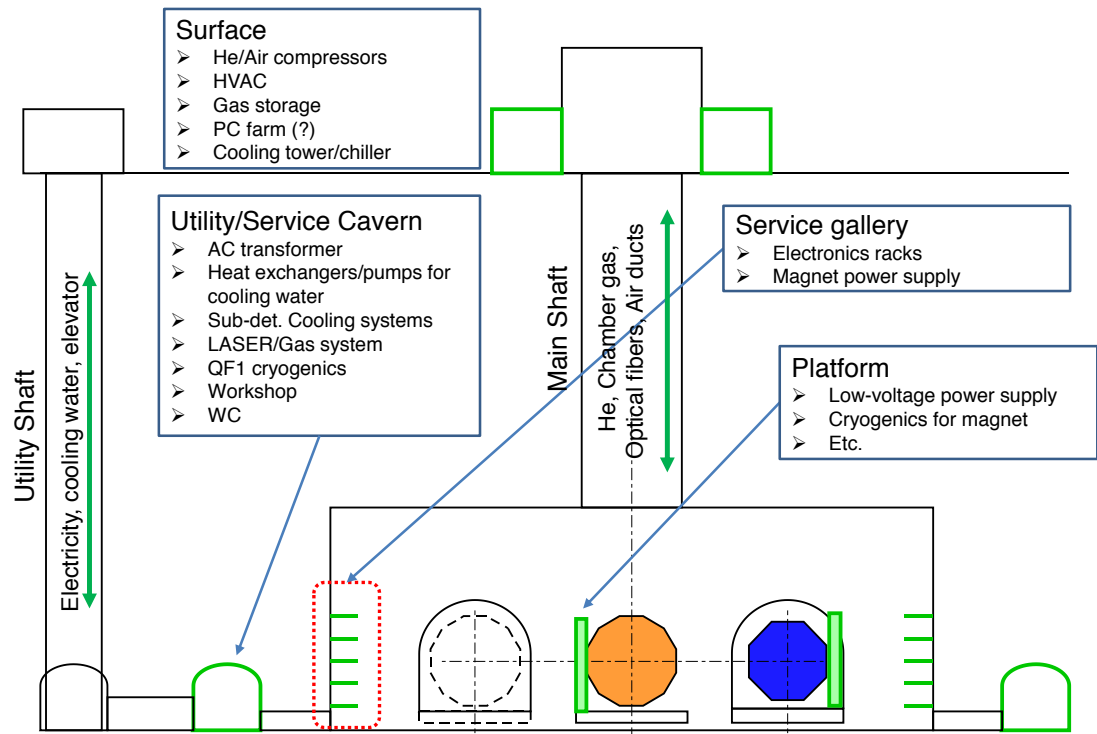


**Figure I-6.4.** Schematic drawing of the possible locations for detector services. The Utility/Service cavern for the detector is proposed but not yet implemented into the ILC design [6].

Yasuhiro Sugimoto

1 pages

### 6.2.2 Cavern ancillary services

Summary of ancillary services from subdetectors in the cavern and on surface, as it will result from subdetector information to be provided in Yasuhiro's excel file.

ILD overall wish for utility space on the platform, the service gallery and the service cavern.

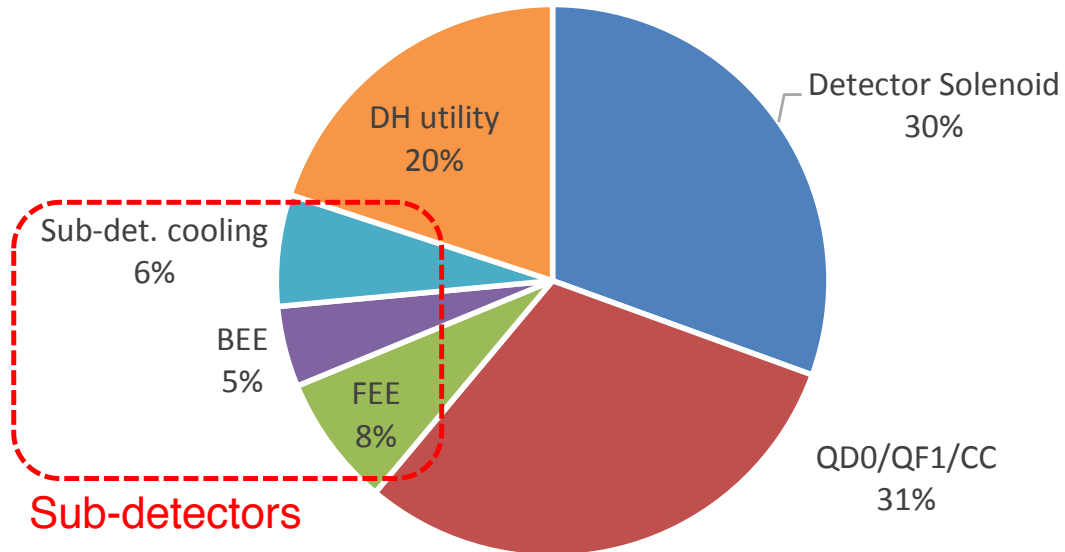


**Figure I-6.5.** Distribution of the underground power consumption for ILD [6]. While the detector solenoid, the machine elements (magnets QD0/QF1 and the crab cavity system CC) use the major part of the power, the detector hall (DH) utilities and the sub-detectors cooling, back- and front-end electronics (BEE, FEE) contribute less. The total power consumption sums up to about 1 MW.

Matthew Wing, Taikan Suehara  
2 pages

### 6.3 Data acquisition

Expected principles and sketch of the DAQ.

Summary of characteristics of subdetector data including data throughput and local filtering, based on DAQ information recently requested to all subdetectors.

EUDAQ developments towards combined DAQ systems for beamtests

Felix Sefkow, Henri Videau,  
Karsten Buesser, Roman  
Poeschl, Toshiaki Tauchi  
3 pages

### 6.4 Mechanical structure and studies

The mechanical behaviour of the ILD components is crucial in two respects. On the one hand, the high-precision and hermeticity of the detector requires a precise relative adjustment of subdetector components within each other, with tight tolerances at the interfaces and boundaries. These aspects were studied by simulating static deformations of the components under gravity and other constraints. On the other hand large devices in Japan must obey strict rules as regards their behaviour in case of seismic events (see section 6.9). This was investigated by modelling the dynamic behaviour of components, including the computation of their "eigen modes" and their reaction to reference earthquake parameters from the foreseen ILC Kitakami site. Most of the attention has up to now been given to the calorimeter mechanical structure which governs the global stiffness of the ILD detector inside the coil. Some evaluations have also started for other subdetectors such as the TPC.

#### 6.4.1 Calorimeter structure

As mentioned in section 5.1.2 two options of the hadronic calorimeter, so-called "Videau" and "TESLA", are under consideration. In both cases, the electromagnetic modules are fixed to the inner plates of the hadronic wheels with two rails parallel to the z direction. Two critical aspects are of

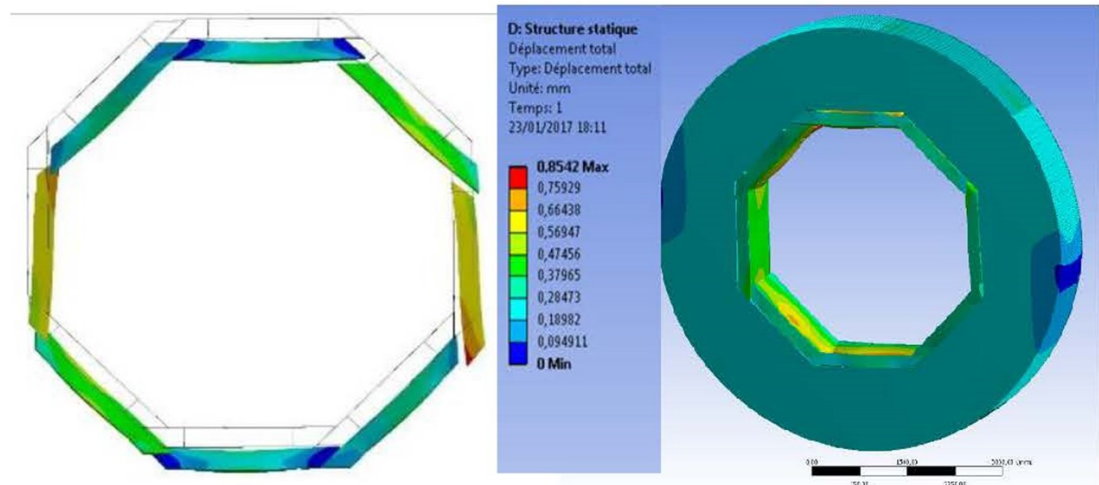


**Figure I-6.6.** Static deformations of the calorimeter "Videau" structure (right) and zoom on the electromagnetic modules displacements with a magnification factor of ??? (left).

particular importance for the calorimeters: the respect of the tolerances of the thin azimuthal clearance (2.5mm) between the electromagnetic modules, to avoid mutual contact and possible damage of the modules, and the flatness of the hadronic absorber plates which define the gaps in which the sensitive layers are introduced. The latter is particularly important for the SDHCAL instrumentation option since RPC's require a high level of flatness. Both Videau and TESLA mechanical options have been simulated in detail and the results provide input for further optimization of the layouts.

**Videau simulations:** The static behaviour of a full Videau calorimeter wheel was simulated with a shell model with ??? nodes. In order to save computing time, the electromagnetic modules were approximated by a 3D solid model. This simplification was validated separately by a comparison to a single module shell model simulation. The results are shown in Figure I-6.6: the hadronic structure turns out to be very stiff with largest deformations of a fraction of a mm. This is due to the vertical flanges of the Videau modules which strongly rigidify the overall structure. The electromagnetic modules are also only slightly distorted: the largest deformation stays below 1mm and the azimuthal clearance between modules is reduced to 2.3 mm in the worst case, well within the required tolerances.

One advantage of the Videau layout is to avoid a projective dead zone at a polar angle of  $90^0$ , but the number of dead zones in  $z$  is 4 for the baseline number of 5 wheels. One question is whether one could reduce this number of dead zones by reducing the number of wheels to 3. Mechanical simulations show that for 3 wheels it is possible to keep deformations at the boundary with the electromagnetic modules within specifications, provided the inner hadronic absorber plate thickness is slightly increased.

First dynamic simulations of the Videau structure were also performed with the computation of eigen modes. They show that the overall calorimeter barrel behaves as a rigid structure under oscillating accelerations, with little variation of the  $z$  distance between the wheels.

**TESLA simulations:** *Static and dynamic behaviour of TESLA structure*

*Comment on LLR-DESY crosscheck.*

### 6.4.2 Other subdetectors

*If available, results on the mechanical behaviour of other subdetectors (e.g. TPC) are also welcome.*

Karsten Buesser, Uwe  
Schneekloth  
3 pages

### 6.5 Coil and yoke studies

Baseline yoke design and discussion of possible lighter options including separation wall option.

Updated field maps for the baseline yoke design. Table of field maps at various locations (including stray fields) for various yoke options.

Progress on technological design of anti-DID (KEK/Toshiba/Hitachi) and corresponding field map.

Daniel Jeans, Yan Benham-  
mou, Sergej Schuwalow,  
Claude Vallee  
2 pages

### 6.6 Beam background studies

The ILD detector response is affected by three main sources of beam-related background: beamstrahlung emitted at the crossing point of the electron and positron bunches, halo muons produced upstream of the detector along the beamline, and low energy neutrons back-scattered from the electron beam dumps. Their impact on the detector occupancies has been quantified and possible mitigation investigated. Results are similar for both options of the ILD detector and are shown here for the large version.

#### 6.6.1 Beamstrahlung

Beamstrahlung consists in  $e^+e^-$  conversion pairs of the photons radiated in the crossing of the dense electron and positron bunches. Most of the low-energy pairs are confined close to the z axis by the large solenoid magnetic field but, due to the crossing angle between the colliding beams, a significant fraction hit the very forward detectors in the region between the incoming and outgoing beam pipes. The central detectors are also affected, both directly by the  $e^+e^-$  pairs, and indirectly through back-scattering of low-energy particles from the forward detectors. It was proposed to mitigate these effects by the addition of a small dipole field to the main solenoidal field. This so-called "anti-DID" field can be tuned to guide the  $e^+e^-$  pairs into the outgoing beampipe.

These effects have been quantified for the updated 250 GeV ILC conditions (ILC250, see chapter 3), using a full simulation of the beamstrahlung particle production and of their tracking within ILD. Special care has been taken to ensure stable results by adapting the GEANT tracking parameters to low energy particles within the beampipe. A realistic field map of both solenoid and anti-DID fields has been used. The response of the most affected detector, the BeamCal, is shown in Figure I-6.7 with and without anti-DID. A positive effect of the anti-DID is clearly visible: when the anti-DID field is applied, the energy distribution is more symmetric around the central beampipe, and its overall amount is reduced by about 30%.

A similar improvement is seen for the central detectors in Figure I-6.8. The most affected are the inner layers of the vertex detector, where the background is equally shared between direct hits rather uniformly distributed, and back-scattered particles showing hot spots in azimuth. Background

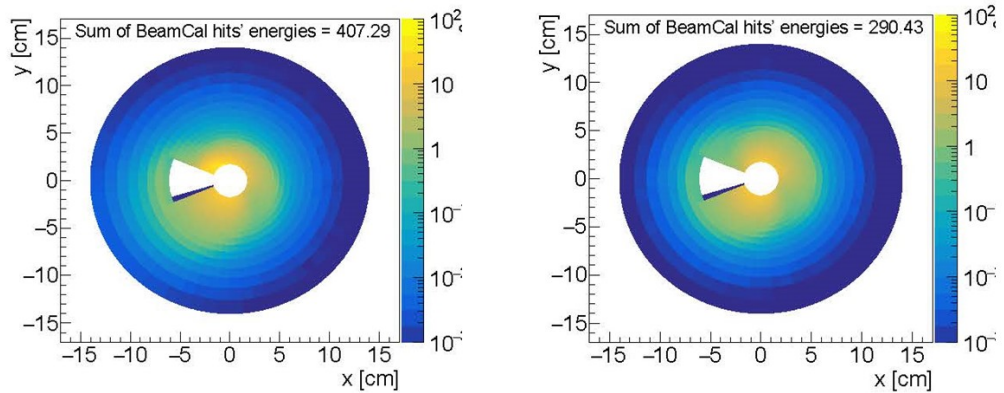


**Figure I-6.7.** Beamstrahlung energy deposition in the BeamCal without (left) and with (right) anti-DID field for the large ILD version at ILC250.

VXD 1	1402 ± 778	914 ± 364
VXD 2	971 ± 558	545 ± 207
VXD 3	151 ± 77	129 ± 60
VXD 4	111 ± 59	107 ± 53
VXD 5	44 ± 30	40 ± 26
VXD 6	39 ± 27	34 ± 24
FTD 1	42 ± 30	38 ± 26
FTD 2	27 ± 19	24 ± 15
FTD 3	62 ± 45	40 ± 27
FTD 4	42 ± 33	25 ± 17
FTD 5	29 ± 23	18 ± 13
FTD 6	16 ± 13	9 ± 7
FTD 7	10 ± 8	6 ± 5
SIT 1	51 ± 37	24 ± 16
SIT 2	49 ± 36	21 ± 12
SIT 3	77 ± 56	34 ± 24
SIT 4	71 ± 54	31 ± 21
SET 1	39 ± 28	15 ± 10
SET 2	46 ± 36	18 ± 12

**Figure I-6.8.** Number of beamstrahlung hits per bunch crossing in the silicon trackers without (left) and with (right) anti-DID field for the large ILD version at ILC250. *Add TPC and transform figure into latex table.*

hits further away from the beampipe are dominated by direct  $e^+e^-$  pairs. The anti-DID has a little effect on direct  $e^+e^-$  hits but efficiently suppresses back-scattered particles and associated hot spots in the central detectors. *Comment also on TPC hits.*

For the small ILD version, the overall beamstrahlung background hit rates are reduced by  $\approx 10\%$  thanks to better confinement within the beampipe by the higher solenoid field of 4T.

*Add info on beamstrahlung effects on beamcal reconstruction and on HCAL occupancy near beampipe*

### 6.6.2 Halo muons

The electrons and positrons of the beam halo produce high-energy penetrating muons parallel to the beam by interacting with beamline components such as collimators. Five magnetized muon spoilers and one optional larger magnetized muon wall are foreseen to deviate these muons outside the ILC experimental hall. The resulting rate of muons in ILD has been simulated for ILC250 and ILC500

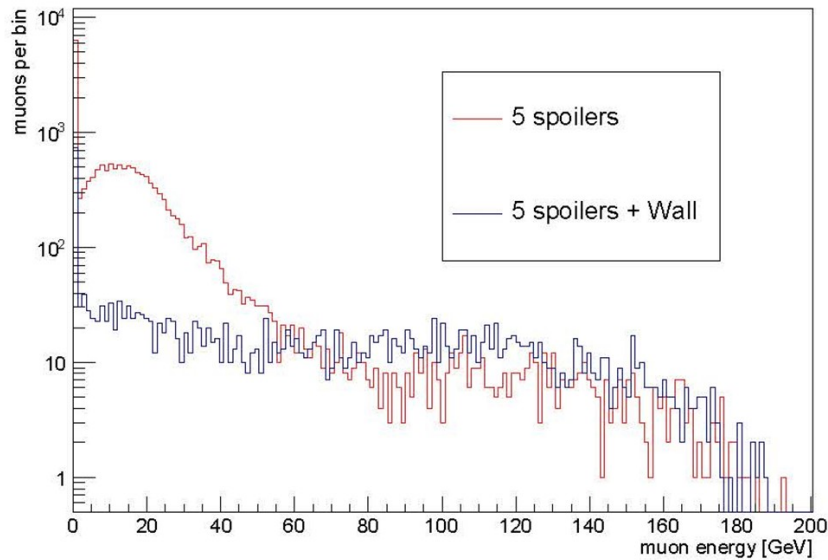


**Figure I-6.9.** Energy spectrum of muons entering the ILC experimental hall for ILC500, normalized to a full single train of 2625 bunches assuming a beam halo fraction of  $10^{-3}$ . Red curve: muon filtering with 5 spoilers only; Blue curve: muon filtering with an additional muon wall.

assuming a beam halo fraction of  $10^{-3}$  (Chapter 3).

Figure I-6.9 shows the energy spectra of the muons crossing the ILD detector for the two filtering options. The muon wall significantly reduces the flux of the lower energy muons below a few 10 GeV. At ILC500 the rate of halo muons crossing ILD is of the order of 4 (resp. 0.6) muons/BC without (resp. with) the optional muon wall. At ILC250 the corresponding numbers are of the order 1 and 0.03 muons/BC for the two filtering options, respectively.

These halo muons will affect the occupancy of the detector but should be easily identified and subtracted from the physics events using topological and timing information.

### 6.6.3 Backscattered neutrons from beam dumps

A potential additional source of beam-related background consists in particles back-scattered from the electron and positron beam dumps located 300m from the interaction point in both beam directions. This background is expected to be dominated by low energy neutrons which can propagate over a long distance. Their contribution has been fully simulated with FLUKA in the context of SiD, including a detailed description of the beamline up to the beam dump as well as of the dump system itself [ref]. The incoming neutron fluxes close to SiD are expected to be the same as for ILD and were interfaced to the ILD detector simulation to estimate their impact in the detector. The simulation was normalized to the dump of one full electron bunch on the  $+z$  side of the detector.

The total number of neutrons reaching the ILD detector region is found to be  $O(10^6)$  per electron bunch dump. These neutrons have very low momenta of a few 10 MeV. Their propagation in ILD was simulated and the map of their stopping points in the detector is shown in Figure I-6.10. The results are in line of what is found for SiD [ref]: most neutrons are absorbed in the external layers of the ILD iron yoke, with a very small fraction reaching the external layers of the very forward calorimeters. Their energy depositions concentrate close to their stopping points: they are very small ( $\approx 0.1$  MIP in average) and asynchronous with respect to the bunch crossings. No visible signal is seen in the ILD vertex detector and central tracker. This indicates that the neutron background should not be a critical issue within its current state of understanding.

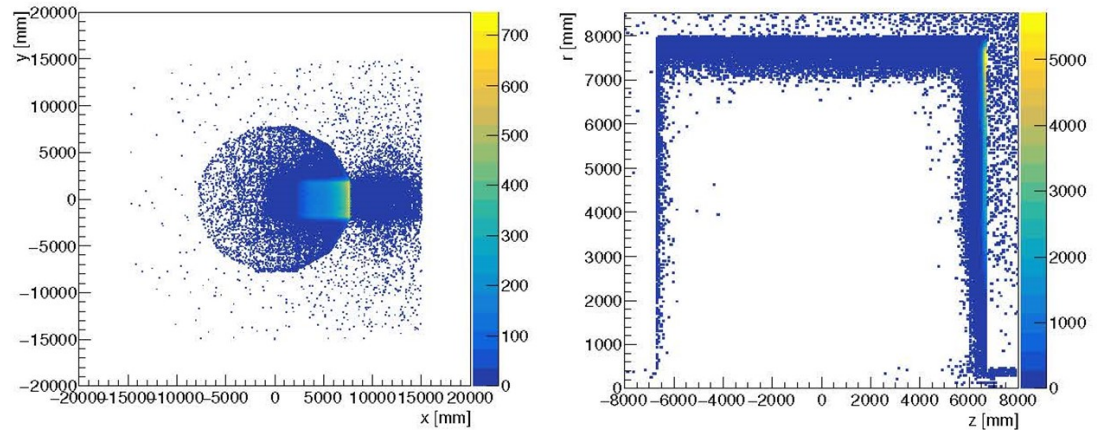


**Figure I-6.10.** Map of the stopping points in ILD of neutrons back-scattered from the beamdump: transverse coordinates (left) and longitudinal coordinates (right). The map is normalized to the dump of one electron bunch on the +z side of ILD.

Graham Wilson

1 pages

## 6.7 Alignment/ calibration procedures

There was little progress here since the LOI/DBD. Most of the corresponding text of these documents could be recovered and summarized for the IDR, taking into account the latest considerations about in-situ calibration with particles/collisions and subdetector requirements.

## 6.8 Technical Documentation

The technical description of the ILD detector concept comprises specification and design documents as well as 3d engineering models, interface descriptions and drawings. All these documents that form the backbone of the ILD technical documentation are stored in the ILC Engineering Data Management System ILC-EDMS [7]. As this powerful system is made for experts and requires appropriate attention, an easy accessible frontend ("EDMSdirect") has been made available. The ILD technical documentation is organised in a Work Breakdown Structure (WBS) that is mapped on a tree browser that can be accessed on the web [8]. Figure I-6.11 shows the tree browser for the ILD technical documentation. All WBS top nodes can be expanded by clicking on them. In the figure, this has been done for the node "Design Integration".

Figure I-6.12 shows the document browser that opens for the documents stored in the EDMSdirect system. Shown here is the "Conventions and Rules" document that belongs to the previous mentioned WBS node "Design Integration". A preview of the document is shown in the document browser. The document browser allows for preview of the respective documents as well as downloads of pdf or source files, depending on the authorisation of the users. Documents can be made worldwide visible as well as protected for selected users.

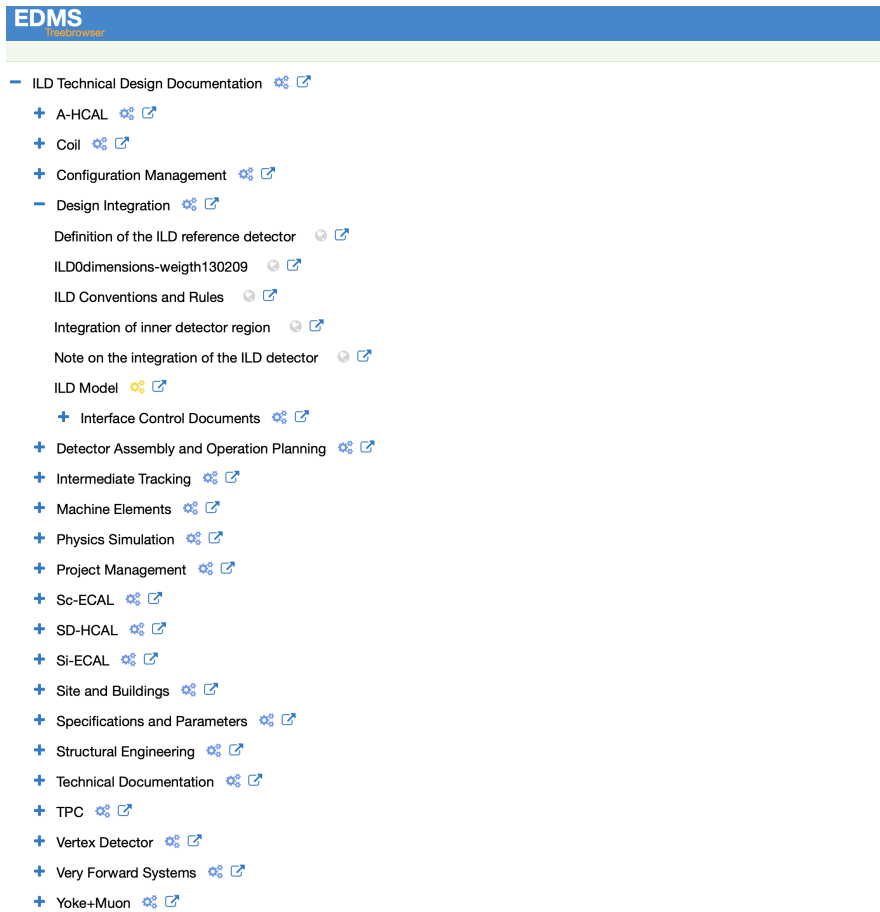


Figure I-6.11. Treebrowser of the ILD technical documentation Work Breakdown Structure in the ILC Engineering Data Management System. The top level node "Design Integration" is shown expanded.

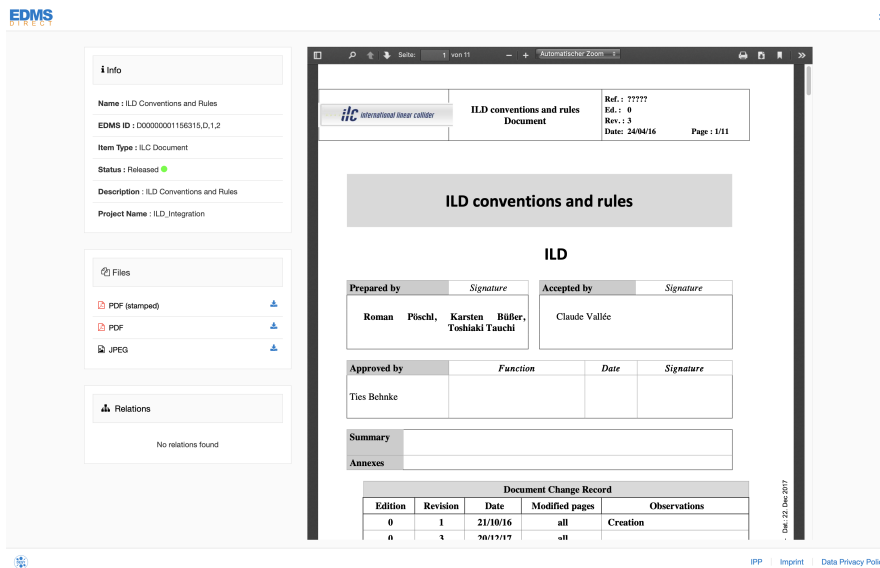


Figure I-6.12. Example document (here:"ILD Conventions and Rules") in the document browser of EDMSdirect.

6.8.1 Interface Control Documents

6.9 Earthquake Safety

Japan is one of most seismically active regions in the world. The proposed sit for the ILC in the Kitakami mountains of northern Honshu has been especially selected putting emphasis on benign

seismic conditions. Earthquake history has been taken into account as well as recent surveys on active tectonic faults. Nevertheless, earthquakes can occur and need to be taken into account. Figure I-6.13 shows all earthquakes that were detected during 30 days in winter 2019/2019 in northern Honshu. The ILD interaction region is in a relatively quiet region around (39N, 141.5E).

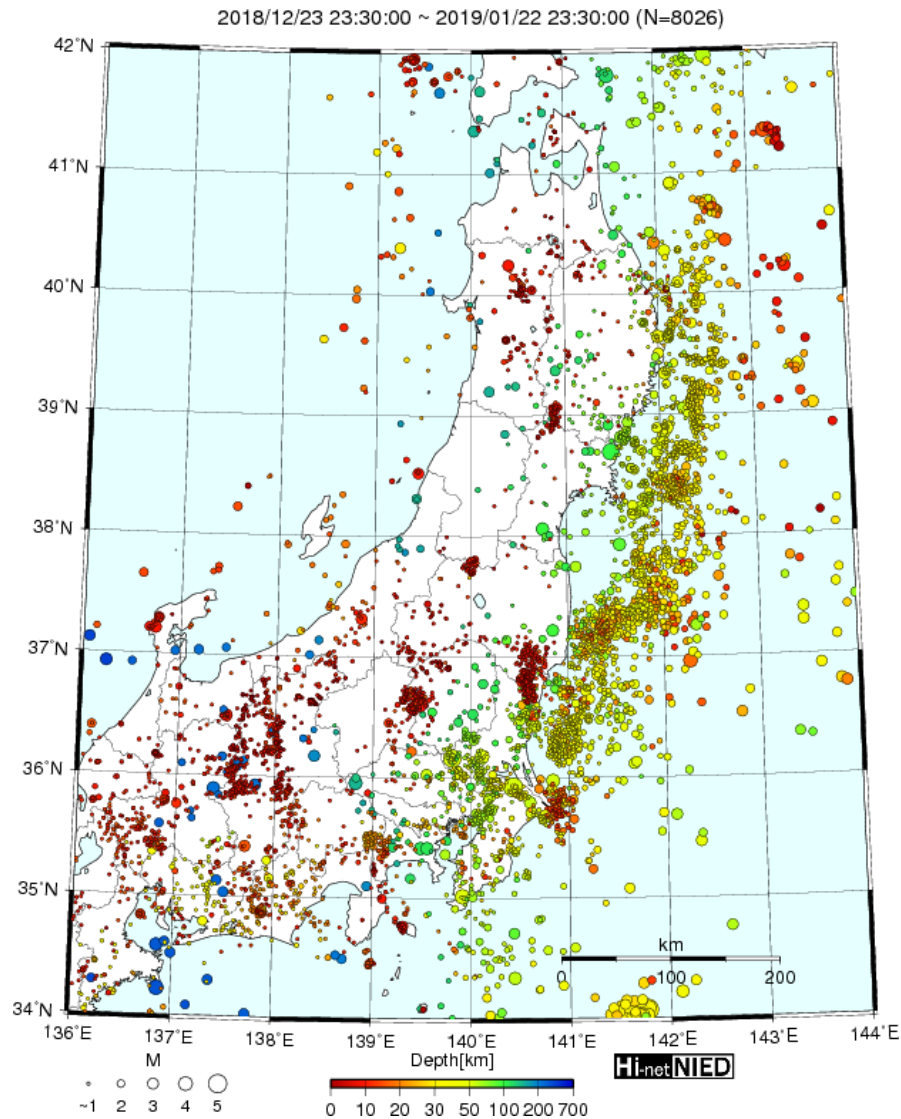


**Figure I-6.13.** Map of northern Honshu with all detected earthquakes between 23rd December 2018 and 23rd January 2019 (30 days) [9]. The ILC interaction region is close to coordinates (39N, 141.5E)

### 6.9.1 Structural Design

Emphasis has been put on the design of the ILD detector with respect to earthquake safety in view of operability of the detector as well as disaster prevention. General rules are provided by the ISO3010 standard: "Bases for design of structures – seismic actions on structures". The ISO standard states two basic principles:

- The structure should not collapse nor experience other similar forms of structural failure due to severe earthquake ground motions that could occur at the site (ultimate limit state: ULS).
- The structure should withstand moderate earthquake ground motions which may be expected to occur at the site during the service life of the structure with damage within accepted limits(serviceability limit state: SLS).

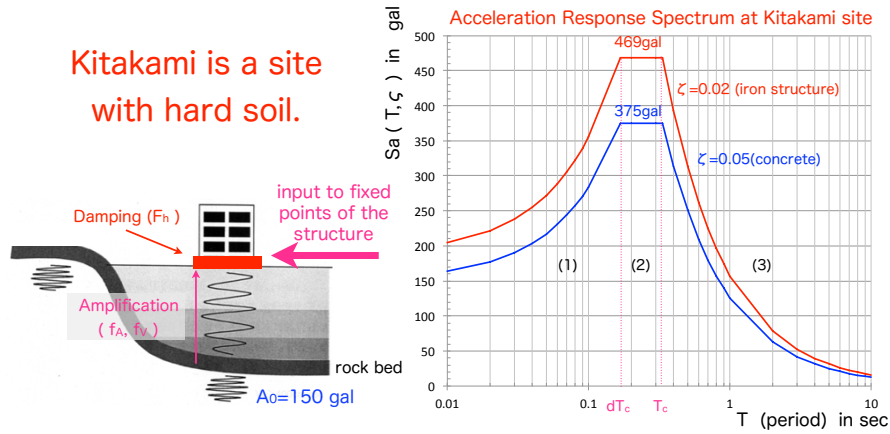


**Figure I-6.14.** Standard response spectra for earthquakes in Kitakami (hard soil) for structures with different damping behaviour [10]. A maximum acceleration of 150 gal for an earthquake with a recurrence frequency of 100 years has been assumed.

As guidance rules, ULS events are those which are expected to happen with recurrence rates of 500 years, while SLS events might happen every 20 years. For the envisaged ILC site in Kitakami this corresponds to maximum expected accelerations of  $\approx 150 \text{ gal}$  and  $\approx 450 \text{ gal}$ .

Proper analysis of the ILD mechanical structures is under way using response spectra for standard earthquakes in Kitakami (c.f. figure I-6.14). Section 6.4 gives an overview of the ongoing structural studies for ILD.

## 6.9.2 Seismic Isolation